

Using CASA IP1 to Diagnose Kinematic and Microphysical Interactions in a Convective Storm

BRENDA DOLAN AND STEVEN A. RUTLEDGE

Department of Atmospheric Science, Colorado State University, Fort Collins, Colorado

(Manuscript received 27 March 2009, in final form 30 October 2009)

ABSTRACT

Data from the Collaborative Adaptive Sensing of the Atmosphere (CASA) Integrated Project I (IP1) network of polarimetric X-band radars are used to observe a convective storm. A fuzzy logic hydrometeor identification algorithm is employed to study microphysical processes. Dual-Doppler techniques are used to analyze the 3D wind field. The scanning strategy, sensitivity, and low-level scanning focus of the radars are investigated for influencing bulk hydrometeor identification and dual-Doppler wind retrievals. Comparisons are made with the nearby S-band polarimetric Next Generation Weather Radar (NEXRAD) prototype radar (KOUN), for consistency. Lightning data are used as an independent indicator of storm evolution for comparison with radar observations.

A new methodology for retrieving the vertical wind utilizing upward and variational integration techniques is employed and shown to illustrate trends in mean wind, with particularly good results at low levels. IP1 observations of a case on 10 June 2007 show the development of the updraft, subsequent graupel echo volume evolution, and a descending downdraft preceded by significant graupel in the midlevels, with updraft and graupel volumes leading the onset of lightning. Many of these trends are corroborated by KOUN. The high temporal resolution of three minutes and near-ground sampling provided by IP1 is integral to resolving up- and downdrafts, as well as hydrometeor evolution. IP1 coverage of the upper levels is diminished compared to KOUN, impacting the quality of the dual-Doppler derived vertical winds and ice echo volumes, although the low-level coverage helps to mitigate some errors. However, IP1 coverage of the low- to midlevels is demonstrated to be comparable or better than coverage by KOUN for this storm location.

1. Introduction

It is estimated that only one-quarter of the troposphere below 3 km is scanned by the current Weather Surveillance Radar-1988 Doppler (WSR-88D) network of radars, given the current radar spacing and earth curvature considerations (McLaughlin et al. 2009). The National Science Foundation (NSF) Engineering Research Center for Collaborative Adaptive Sensing of the Atmosphere (CASA) seeks to employ new low-cost, short-range, adaptively scanning networks of radars aimed at improving low-level sampling of the atmosphere (McLaughlin et al. 2009). To accomplish this, compact X-band radars have been designed to operate on cell phone towers and similar structures. The first radar test bed, known as Integrated Project 1 (IP1), consists of a network of four X-band, Doppler,

polarimetric radars in southwestern Oklahoma (Fig. 1). Although X-band radars were chosen for their compact nature, shorter wavelengths have disadvantages such as non-Rayleigh scattering and attenuation. At times these can become significant, hindering the analysis and even detection of meteorological echoes.

Perhaps the most unique feature of the IP1 radars is their ability to adaptively scan storms in real-time using the so-called distributed collaborative adaptive sensing (DCAS) technology, which determines how to scan the radars based on the current weather situation within the IP1 network (McLaughlin et al. 2009). A Meteorological Command and Control (MCC) determines the type of echoes in the network based on storm identification algorithms, then allocates radars and coordinates scanning between radars to best sample those features (Zink et al. 2008). The rapid and adaptive scanning strategy can optimize the scanning for particular types of meteorological events and change in real time to accommodate changing weather situations. This means that during each volume scan interval the sector size, number of

Corresponding author address: Brenda Dolan, Dept. of Atmospheric Science, Colorado State University, Fort Collins, CO 80523-1371.

E-mail: bdolan@atmos.colostate.edu

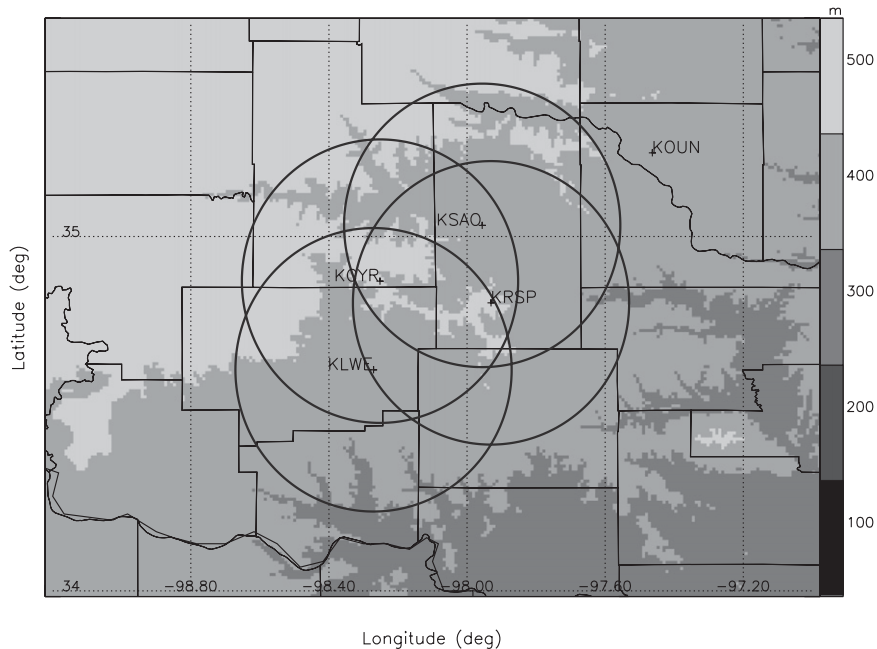


FIG. 1. The CASA IP1 network of X-band polarimetric radars and the NSSL polarimetric S-band radar, KOUN. The 30-km maximum range rings of the IP1 radars are illustrated, and the local topography in meters is shaded.

elevation angles, and focus area can change. For a more extensive description of the MCC, the reader is referred to Zink et al. (2008) and McLaughlin et al. (2009).

Although potential advantages of a low-looking radar network in Oklahoma include improved tornado detection and forecasting, the IP1 network possesses several qualities that could be beneficial for studying more general storm morphology. The network configuration of the IP1 radars allows for the retrieval of three-dimensional (3D) winds using dual-Doppler techniques within the dual-, triple-, and quad-Doppler coverage areas. Furthermore, the dual-polarization capabilities of IP1 can be used to estimate bulk hydrometeor types in order to study microphysical processes. The additional sensitivity of the specific differential phase at X-band aids in correcting attenuation (e.g., Park et al. 2005), and brings the possibility of phase-based rain-rate estimation to lighter rain rates (e.g., Matrosov et al. 2002, 2006). IP1 therefore provides an opportunity to study storm morphology, kinematics, microphysics, and rainfall estimation on time scales of several minutes with high-resolution data focused on the lowest levels of the atmosphere. The increased temporal resolution of IP1 (1 to 3 min) also has a potential for relating radar-derived microphysics and dynamics to lightning and electrification.

This study aims to investigate the capabilities of the IP1 network for convective-scale studies of kinematic

and microphysical interactions. In particular, the ability to retrieve the 3D wind field using dual-Doppler techniques is examined in relation to the limited coverage area and adaptive scanning strategy. Microphysical retrievals are compared with a nearby S-band polarimetric radar [KOUN, operated by National Oceanic and Atmospheric Administration (NOAA)/National Severe Storms Laboratory (NSSL)] in order to draw conclusions about what information the X-band network might provide over more conventional, longer wavelength radars and place the IP1 observations in a larger context. A case collected on 10 June 2007 has been analyzed to demonstrate a storm morphology study using the IP1 network. Lightning data are also examined to provide an independent measure of storm evolution.

2. Data and methodology

a. Radar

During the 10 June 2007 case, all four IP1 radars were fully operational and employed adaptive scanning techniques. For this case, the scan update cycle time, or “heartbeat,” was chosen to be three minutes in order to accommodate more scanning elevations to maximize coverage of the highest regions of the storm while still maintaining an update time less than that of the current WSR-88D S-band network of radars. The scan volume

start times of the radars are coordinated to within a few seconds by the MCC. During each three-minute heartbeat, a 360° surveillance scan was performed at 2° elevation to provide a general overview of activity in the network. The MCC selected sector sizes for the other elevation angles based on the size of the echo in each radar view, and depending on the sector size, volume scans utilizing 4 to 12 elevation sweeps between 1° and 31° (the upper limit is a design consideration) were conducted. The possible elevation angles are illustrated in Fig. 2a. Here we note that angles were selected from bottom to top such that the low elevation angles were used in every scan and higher elevation angles were included when time permitted. For the case presented here, the range of the radars was limited to 30 km in order to accommodate the large volume of data transmitted through the network. The IP1 radars are mechanically scanning with a half-power beamwidth of 1.8° and employ a dual-pulse repetition frequency (PRF) waveform at 2.4 and 1.6 kHz, resulting in a combined maximum unambiguous velocity of 38 m s^{-1} .

The IP1 data were subjected to a variety of quality control measures. The data processing methodology is described in Fig. 3. Reflectivity data were corrected for attenuation using a network-based attenuation correction (Chandrasekar and Lim 2008). This method of attenuation correction, called the network-based retrieval system (NRS), is based on the principle that for a set of radars, differences in observed reflectivity in a common volume are due to the path integrated attenuation. Specific attenuation and reflectivity are retrieved through minimization of a cost function using all the radar observations in common volumes (Chandrasekar and Lim 2008). Several types of analyses were performed to evaluate the attenuation correction algorithms. First, reflectivities from the IP1 radars were compared with local NEXRADs and KOUN data. Second, a consistency test between Z and differential phase ϕ_{dp} was compared to a theoretical $Z-\phi_{dp}$ line. Both of these tests indicated better performance by the NRS than a self-consistent method using specific differential phase (Park et al. 2005; Gorgucci et al. 2006), possibly because of contamination from melting ice. Differential reflectivities were corrected using the specific differential phase in a self-consistent manner (Park et al. 2005; Gorgucci et al. 2006). Additionally, radar differential reflectivity biases were estimated using data from the trailing stratiform region of a meso-scale convective system (MCS) on 20 June 2007. A region of assumed spherical particles where Z_{dr} should be 0 dB was used to determine the offset for each radar. Biases were found to be on the order of several tenths of a dB for individual radars.

Once the data were corrected for attenuation effects and radar biases, they were quality controlled using

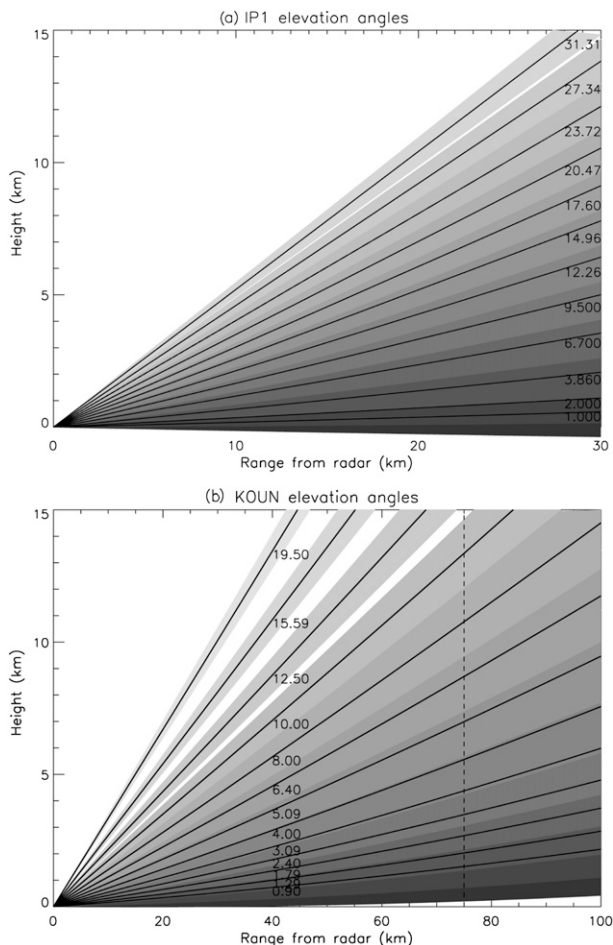


FIG. 2. Elevation angles used in the scanning sequence for (a) IP1 with a half power beamwidth of 1.8° and (b) KOUN with a half-power beamwidth of 1° during the 10 Jun 2007 case. The dashed line in (b) denotes the distance to the center of the IP1 network.

polarimetric-based thresholds on correlation coefficient (ρ_{hv}) and standard deviation of ϕ_{dp} (Ryzhkov and Zrnic 1998). A sensitivity study was performed to determine the appropriate thresholds, and for this case data were thresholded on ρ_{hv} less than 0.5 and standard deviation [$Sdev(\phi_{dp})$] $> 25^\circ$ on a gate-to-gate basis (Fig. 3).

The quality-controlled data were gridded to a $0.5 \times 0.5 \times 0.5 \text{ km}$ Cartesian grid using a Cressman weighting scheme (Fig. 3), centered on a common point in the center of the network. Because any single radar in the network may only provide an incomplete picture of the entire storm at any given time, reflectivity (Z_h), Z_{dr} , K_{dp} , and ρ_{hv} from the four radars were merged by taking the highest value at each grid point (Fig. 3). It is noted that this technique can introduce false boundaries and artifacts if the calibration of any of the radars is not similar to the others, but we feel that this technique provides more information than considering only individual radars and

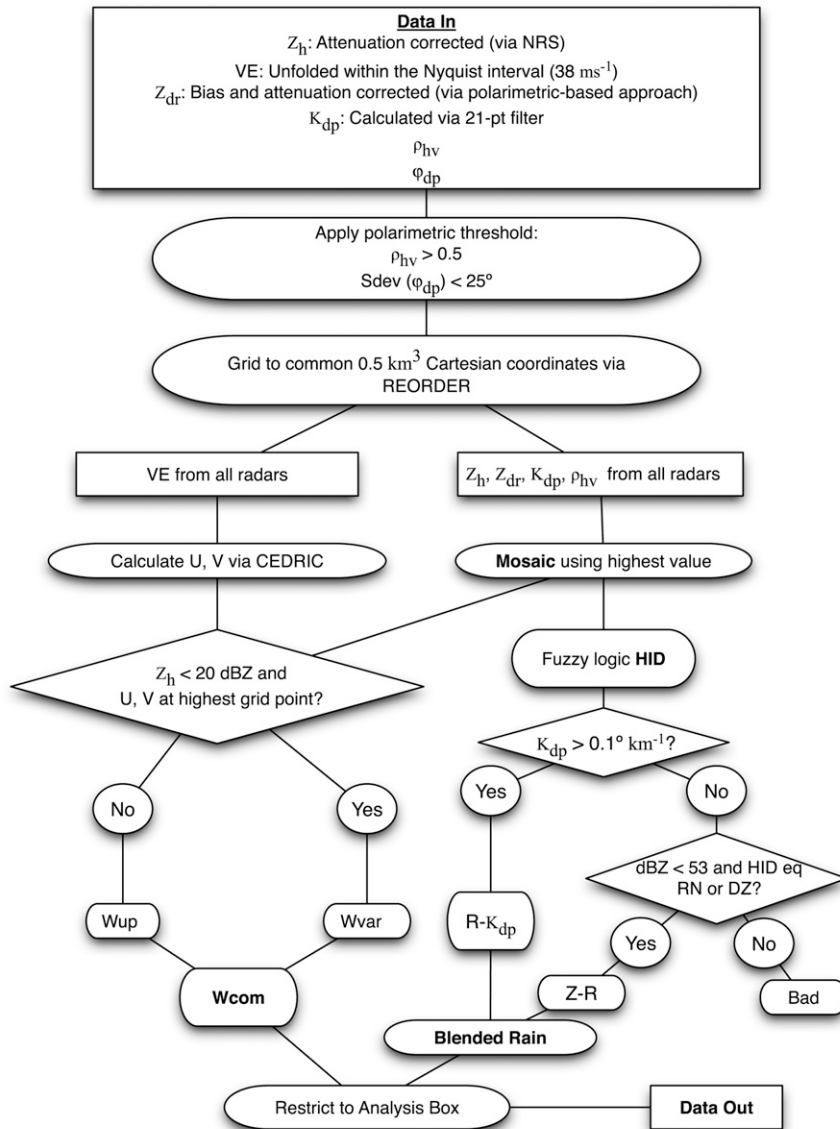


FIG. 3. Methodology for quality controlling and processing IP1 data.

greatly simplifies the analysis. All IP1 images in this study represent the merged product derived from all four radars.

KOUN is an S-band, polarimetric radar located approximately 75 km from the center of the IP1 network (Fig. 1), providing an essentially nonattenuating (11 cm) source and a more conventional “sit and spin”-type scanning strategy for comparisons. KOUN scans 360° full volumes with 13 elevation angles up to 19.5° approximately every 5 min. (Fig. 2b). The half-power beamwidth of KOUN is 1° (Ryzhkov et al. 2005). KOUN data were quality controlled using thresholds of 0.6 for ρ_{hv} and 18° for $Sdev(\phi_{dp})$. Because of beam

geometry resulting from the distance between KOUN and the IP1 network, KOUN data were gridded to a coarser grid (1.0 km × 1.0 km × 1.0 km) using Cressman weighing and the same center as IP1.

b. Lightning

Data from the National Lightning Detection Network (NLDN; Cummins et al. 1998) provided cloud-to-ground (CG) flash rates, as well as CG polarity (positive or negative). Cummins et al. (1998) estimates the detection efficiency of the NLDN over southwestern Oklahoma at 80%. Location errors are on the order of 1–2 km.

TABLE 1. List of hydrometeor categories used in the fuzzy logic HID scheme. For more details of the HID used in this paper, the reader is referred to Dolan and Rutledge (2009).

HID category	Short name
Drizzle–light rain	DZ
Rain	RN
Aggregates	AG
Ice crystals	CR
Low-density graupel	LDG
High-density graupel–small hail	HDG
Vertically aligned ice crystals	VI

The Oklahoma Lightning Mapping Array (OK-LMA) detects the location of radiation sources from lightning in the VHF portion of the electromagnetic spectrum. These sources can then be grouped temporally and spatially into lightning flashes thereby providing an estimation of intracloud (IC) flash rates (Thomas et al. 2003). A description of the LMA instrumentation and application can be found in Rison et al. (1999) and Thomas et al. (2004). Between the NLDN and OK-LMA, the total flash rate (TFR), CG flash rate, and IC flash rates can be estimated.

The charge structure of a storm can be inferred from OK-LMA data if assumptions are made about the nature of breakdown in lightning strikes (Rust et al. 2005; Wiens et al. 2005). The so-called bidirectional breakdown model hypothesizes that breakdown begins between two regions of opposite charge (Kasemir 1960; Williams et al. 1985; Rison et al. 1999; Mansell et al. 2002). The discharge then propagates away from the initial origin with two leaders in opposite directions, a negative leader moving toward positive space charge (negative breakdown) and a positive leader moving toward negative space charge (positive breakdown). Rison et al. (1999) showed that in the VHF, negative breakdown is inherently noisier than positive breakdown, and as such, regions of positive charge have more VHF sources compared to regions of negative charge. Therefore by examining source densities and initial discharge heights and breakdown profiles of individual lightning flashes captured by the LMA, the general nature of charge regions can be inferred.

c. Algorithms

A fuzzy logic hydrometeor identification (HID) algorithm based on theoretical simulations of scattering properties of various hydrometeor types was used for both S- and X-band (Dolan and Rutledge 2009; Fig. 3). The HID algorithms include seven hydrometeor types (Table 1): drizzle/light rain (DZ), rain (RN), aggregates (AG), pristine ice crystals (CR), low-density graupel (LDG), high-density graupel–small hail (HDG), and vertically aligned ice crystals (VI). Hail categories were not considered because of the complicated non-Rayleigh

and attenuation effects at X-band. The case presented here was specifically chosen because of the presence of only small amounts hail (identified by an S-band HID including hail categories applied to KOUN) to minimize these complications. Details of the HID method can be found in Dolan and Rutledge (2009). HID will be used to infer bulk microphysical processes occurring within the storm.

The theoretically based HID was applied to gridded, mosaicked IP1 (Fig. 3) and gridded KOUN data. Hydrometeor echo volumes were derived by multiplying the number of points identified as a certain hydrometeor type by the grid size ($0.5 \times 0.5 \times 0.5 \text{ km}^3$ in the case of IP1 and $1.0 \times 1.0 \times 1.0 \text{ km}^3$ in the case of KOUN). Areas were calculated in the same manner, but to provide a consistent comparison, KOUN data were interpolated to the same vertical spacing as IP1 (0.5 km).

The arrangement of the IP1 network affords the opportunity for dual-Doppler wind synthesis in order to estimate the 3D wind field. Adaptive scanning techniques included targeted scanning (scanning in the same area at the same time by more than one of the IP1 radars) in the multi-Doppler areas, coordinated volume starting times to minimize errors from advection and storm evolution, as well as possible elevation angles up to 31° in order to try to “top” the storms of interest (Wang et al. 2008).

The horizontal wind field is derived through a vector decomposition of two or more radial velocity observations. Ray et al. (1980) and Kessinger et al. (1987) showed that the addition of radars contributes to reducing the error variance. Errors associated with the horizontal wind field estimation are on the order of 1 m s^{-1} (Doviak et al. 1976; Kessinger et al. 1987). Vertical velocities (w) are often arrived at through integration of the continuity equation, which requires assumptions about particle fall speeds and boundary conditions. Depending on the boundary conditions that are known, integration can proceed from the surface to the echo top (upward integration W_{up}) or from the echo top to the surface (downward integration). O’Brien (1970) showed through consistency arguments that any residual errors from a downward integration at the surface can be redistributed throughout some assigned portion of the column to ensure the bottom boundary condition ($w = 0$) is satisfied, termed variational integration (W_{var}). Several studies have examined the errors associated with different vertical motion retrieval methodologies (Bohne and Srivastava 1976; Ray et al. 1980; Nelson and Brown 1987; Matejka and Bartels 1998) and found W_{var} to be superior to W_{up} under most circumstances. This is because of density stratification in the atmosphere that leads to compounding errors when integration proceeds from the surface to the echo top. However, Ray et al. (1980) demonstrated that for W_{var} , errors

resulting from inaccuracies associated with the upper boundary condition will damp out with decreasing height, but inaccurate surface boundary conditions can introduce errors. However, Nelson and Brown (1987) found that incomplete sampling of the upper and lower boundaries were not dominant sources of error for W_{var} . Finally, Ray et al. (1980) and Matejka and Bartels (1998) found that errors with W_{up} are generally small below about 4 km, and errors with W_{var} can be excessive when the top and bottom boundary conditions are significantly inaccurate.

Despite the availability of relatively high elevation angles and targeted multiple-Doppler scanning techniques implemented for this case, echoes were not always topped by two or more radars. To balance significant errors resulting from incomplete sampling of the upper boundary condition with unconstrained and anomalous winds arising from upward integration techniques, a combined method of determining the vertical component of the wind was developed (W_{com}). The type of integration used is determined on a column-by-column basis depending on if the storm was topped by two or more radars. In the case of the IP1 radars, a storm was assumed “topped” if the reflectivity at the highest grid point containing data was <20 dBZ and was scanned with two or more radars. If the criterion for topping the storm was met, then W_{var} was used, otherwise W_{up} was selected (Fig. 3). Obviously, a lower reflectivity threshold is desirable for detecting echo top, but because of the radar sensitivity and attenuation effects, 20 dBZ had to be used. However, as shown in Ray et al. (1980) and Matejka and Bartels (1998), accuracy of the upper boundary condition contributes much less to overall errors than knowledge of the lower boundary condition where density is greatest. Similarly, upward integration retrievals will be much more accurate with better sampling of the low levels. In the case of the IP1 radars, the bottom boundary condition is always within 200–300 m of the surface. Thus, we feel confident that a 20-dBZ echo-top height results in relatively small errors that dampen with height, and that W_{up} can accurately retrieve vertical winds in the lowest several km. We will assess the performance of W_{com} further in section 3b. Winds were synthesized using National Center for Atmospheric Research (NCAR) Custom Editing and Display of Reduced Information in Cartesian space (CEDRIC) program (Mohr and Miller 1983; Fig. 3). The 700-mb “steering wind” from the 1200 UTC KOUN sounding (13 m s^{-1} from 210°) was used for storm advection in the dual-Doppler analysis.

For the purposes of this study, rain-rate estimation R was used only for distinguishing areas of heavy, moderate, and light rainfall. A blended algorithm using HID, Z - R , and relationships was employed for rain rate estimation at X-band (Fig. 3). To take advantage of the

Oklahoma-tuned R - K_{dp} determined during the Joint Polarization Experiment at S-band (Ryzhkov et al. 2003), the R - K_{dp} was scaled with frequency from S-band to X-band (Bringi and Chandrasekar 2001).

$$R = 17.38K_{\text{dp}}^{0.786}. \quad (1)$$

If $K_{\text{dp}} > 0.1^\circ \text{ km}^{-1}$, then the R - K_{dp} relationship was used. If $K_{\text{dp}} < 0.1^\circ \text{ km}^{-1}$ and HID identified the gridpoint as either RN or DZ, then the NEXRAD Z - R relationship was used (Fulton et al. 1998):

$$R = 0.017Z_h^{0.714}. \quad (2)$$

And finally, if HID identified any ice category at a gridpoint with $K_{\text{dp}} < 0.1^\circ \text{ km}^{-1}$, then the gridpoint was assumed to be contaminated by ice and a rain rate was not calculated (see Fig. 3). A similar blended algorithm utilizing Z_h , Z_{dr} , and K_{dp} was employed for KOUN using the relationships outlined in Ryzhkov et al. (2005) with the decision tree discussed in Cifelli et al. (2002).

3. Analysis

a. Case overview

On 10 June 2007, a multicellular storm developed to the southwest of IP1 and moved through the network to the northeast, allowing IP1 to capture nearly the entire 2.5-h lifetime of the storm. The storm entered the IP1 network around 2252 UTC as several reflectivity cores (Fig. 4a) that eventually joined to form a linear complex by 2318 UTC (Fig. 4b). After 2320 UTC, the storm began to separate into two reflectivity cores, one to the southwest (A) and one to the northeast (B). Cell A reached a reflectivity maximum at 2340 UTC, and rapidly dissipated after 0000 UTC 11 June 2007 while cell B intensified around 2347 UTC (Fig. 4c) and continued to remain vigorous past 0001 UTC 11 June 2007 (Fig. 4d). Because of the proximity to other storms on this day (not shown), a moving analysis box was drawn around the storm complex¹ of interest and all data were then limited to within that domain.

No severe weather was reported for this storm complex. Despite only limited pockets of large and small hail identified by KOUN, non-Rayleigh influences on X-band reflectivity were noted, as evidence by maximum reflectivities of >65 dBZ for KOUN and >75 dBZ for IP1. Nonetheless, these effects were limited in space and time, making this an ideal case to study.

¹ Herein, “storm complex” will be used to define the entire storm, from 2230 to 0030 UTC, encompassing the time before splitting as well as cells A and B.

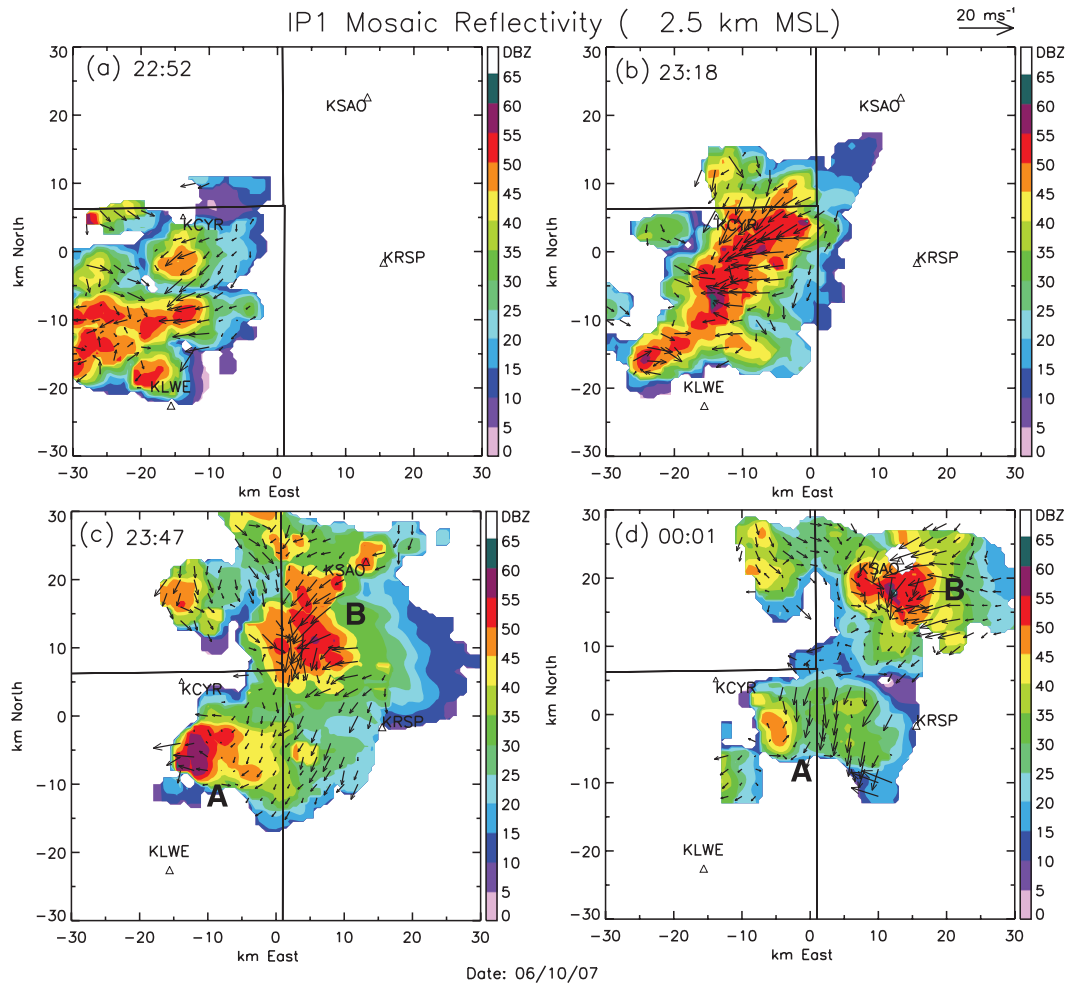


FIG. 4. Horizontal cross section of IP1 reflectivity at 2.5 km MSL for four different times (a) 2252 UTC 10 Jun 2007, (b) 2318 UTC 10 Jun 2007, (c) 2347 UTC 10 Jun 2007, and (d) 0001 UTC 11 Jun 2007. Storm-relative dual-Doppler-derived winds are overlaid. The relative locations of the two cells discussed in the text are indicated with “A” and “B”, and the IP1 radar locations are indicated with triangles.

To understand the impact of radar coverage area on the results discussed below, the relative echo area of IP1 reflectivities >20 dBZ was compared to the total reflectivity area >20 dBZ observed by KOUN (Fig. 5a). Because of scanning considerations, IP1 has limited coverage (10%–40%) of heights above 3 km until approximately 2300 UTC when IP1 scanning began to cover 60%–90% of the upper levels. The best coverage occurs between 2315 and 0000 UTC. Figure 5b illustrates the dual-Doppler coverage area compared to the IP1 reflectivity area >20 dBZ. During the early (2200–2230 UTC) and late (2350–0030 UTC) periods of the storm complex, dual-Doppler analysis could be performed on nearly the entire area covered by IP1. Between 2230 and 2350 UTC, a large volume of the storm complex passed through the KLWE–KCYR and KSAO–KRSP baselines, where winds could not be retrieved. This

results in dual-Doppler wind retrievals in only 25%–75% of the IP1 area, with particularly degraded coverage in heights above 5 km. The variable IP1 coverage area will influence the ability to retrieve the wind field and impact quantitative analysis. We will assess the W_{com} methodology and analyze the resulting dynamics of the 10 June 2007 storm complex in section 3b. The HID will be examined and used to infer bulk microphysics in section 3c, and we will relate the radar observations to lightning observations for a combined analysis in section 3d.

b. Kinematic analysis

To estimate the uncertainties that might be associated with using W_{up} , the difference between the vertical wind determined from W_{up} and W_{var} in each “topped” column was calculated. Differences between the two will provide an estimate of the errors that result from using W_{up}

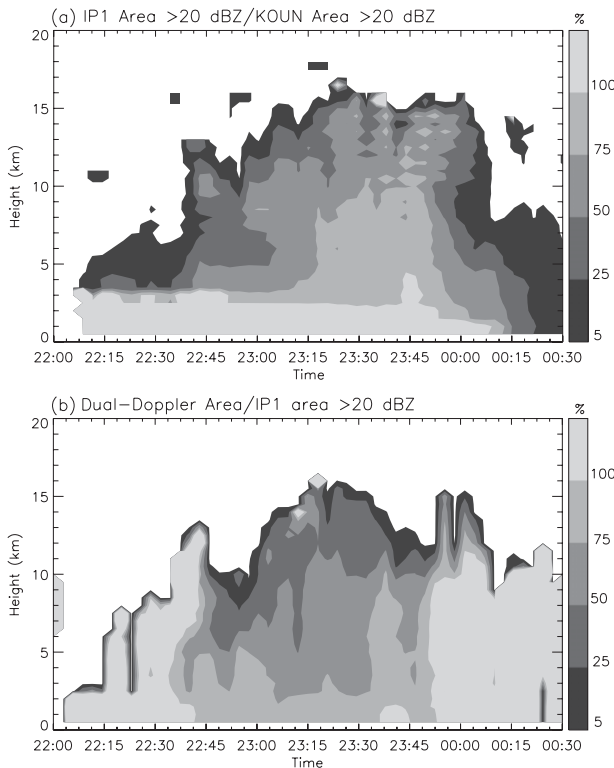


FIG. 5. Time–height cross section of (a) percentage of IP1 area >20 dBZ compared to KOUN area >20 dBZ, and (b) percentage of dual-Doppler coverage as a function of IP1 reflectivity area >20 dBZ.

instead of W_{var} , which is generally accepted as being more accurate than W_{up} (Bohne and Srivastava 1976; Ray et al. 1980; Matejka and Bartels 1998). The mean vertical wind at two different times is shown in Fig. 6. At 2229 UTC, the overall mean difference between using the W_{up} and W_{var} methods was 0.8 m s^{-1} (Fig. 6a), while at 2338 UTC this difference was slightly larger at 1.2 m s^{-1} (Fig. 6c). The overall mean wind trends are generally preserved, although at 2229 UTC, the W_{var} method indicates upward motion in the midlevels while W_{up} shows downward motion in the same area. Mean profiles at 2338 UTC match generally better than at 2229 UTC with the exception of a large spike in negative velocities above 9 km when using the W_{up} integration method, illustrating one of the main problems associated with using upward integration (unconstrained accumulation of errors at the upper boundary). If the mean profiles are divided into the up and down components (Figs. 6b,d), the relative error associated with the up- and downward motion can be estimated. In both cases, the upward vertical motion has a smaller relative error (0.8 and 0.9 m s^{-1} at 2229 and 2338 UTC, respectively) than downward motion (1.8 and 1.3 m s^{-1} at 2229 and 2338 UTC, respectively). It is also

clear that differences are smaller below about 6 km and become very large, especially in the case of downward motion, above 8 km. These conclusions are supported by the findings of Ray et al. (1980) and Matejka and Bartels (1998) that W_{up} performs reasonably well at low levels. Again, in the lower and midlevels, trends in vertical motion with height are persevered between the two integration methods. This leads us to conclude that although there can be large differences between W_{up} and W_{var} , general tendencies (i.e., location and timing of updraft and downdraft), particularly below about 8 km, can still be inferred. Since there are clearly large errors in wind magnitudes associated with using W_{up} , as well as the threshold of 20 dBZ for W_{var} columns, we have determined not to focus on magnitude metrics such as maximum updraft speed, but rather up- and downdraft areas that meet certain criteria.

The mean w derived from W_{com} at different times throughout the observation time period are shown in Fig. 7. At 2310 UTC when the storm complex is initially developing, a large layer of mean upward motion is noted in the midlevels between 4 and 8 km (Fig. 7a). Large negative w above 10 km are likely an artifact of the columns using W_{up} . Twenty-five minutes later, at 2338 UTC, the profile indicates that the mean upward motion has weakened and extended slightly higher to 10 km. By 0012 UTC, the mean vertical motion is dominated at all levels by downward motion (Fig. 7a). During lifetime of the storm complex, mean upward speeds below 10 km peak at 7 m s^{-1} , while mean downward speeds below 10 km peak at 9 m s^{-1} (Fig. 7b). Both up- and downdraft speeds increase with height, likely resulting from columns using W_{up} . Low-level speeds are on the order of $2\text{--}3 \text{ m s}^{-1}$, while midlevel speeds range from $3\text{--}7 \text{ m s}^{-1}$ for both upward and downward motion (Fig. 7b).

An example of storm-relative dual-Doppler derived winds is shown in Fig. 8. The column-by-column integration method selected for W_{com} (Fig. 3) is also illustrated (Figs. 8b,d). The surface flow at 0.5 km MSL (200–300 m AGL; Figs. 8a,b) shows converging wind on the southeast flank of cell B, with inflow from the northeast. The air then exits the main updraft to the south. Dual-Doppler coverage at this time in the southern part of the storm complex was sufficient to use W_{var} in most columns (Figs. 8b,d), likely because of the generally lighter reflectivities and lower storm tops. Throughout the middle of the network, the W_{up} methodology had to be used because of incomplete topping of the main reflectivity core, with W_{var} used around some of the edges. The radar baselines are also clear, where no winds can be retrieved (indicated by “no retrieval” NR in Figs. 8b,d). A vertical projection along the cross section at $x = 0$ (Figs. 8c,d)

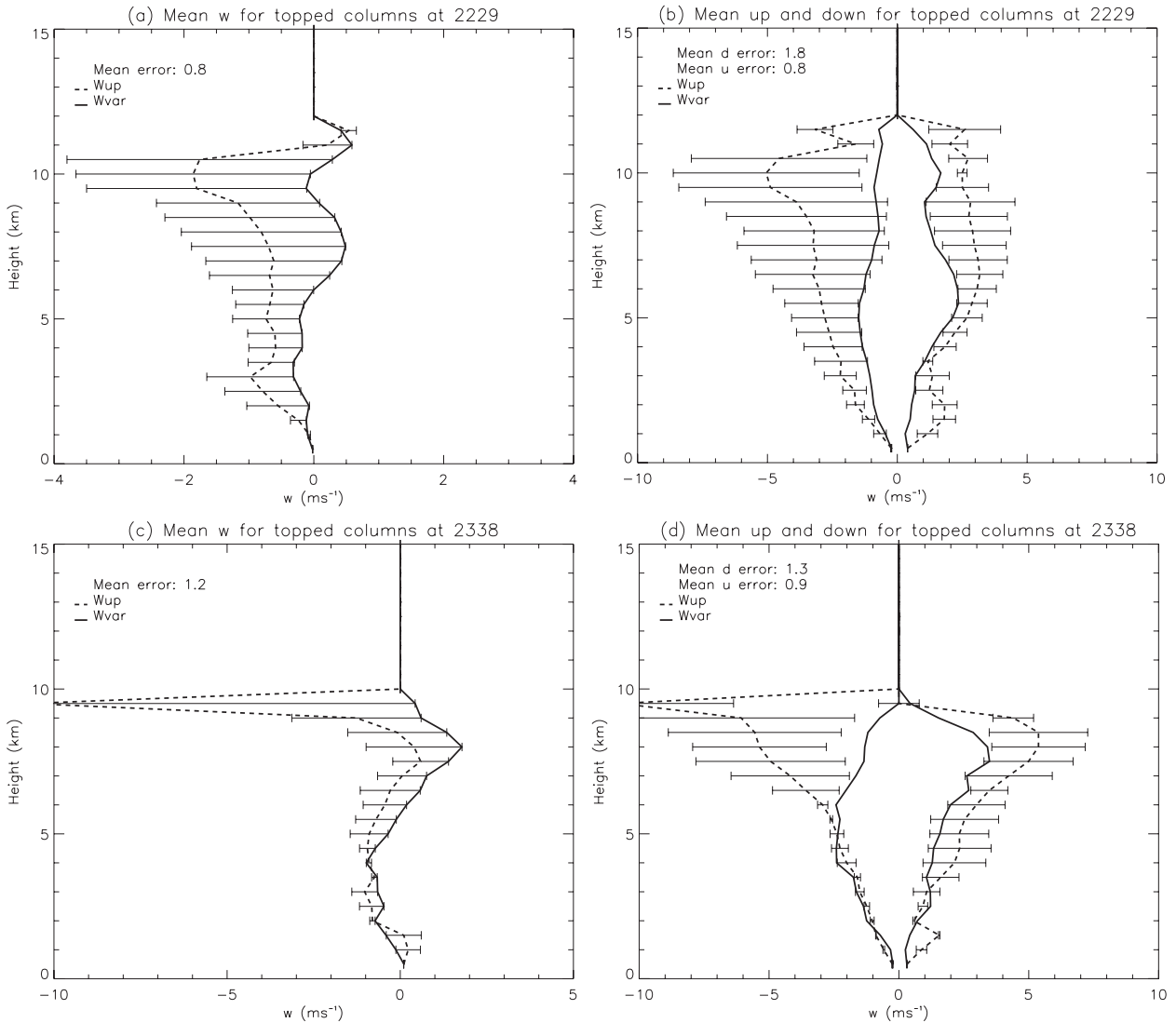


FIG. 6. Comparison of mean vertical motion (w) derived from W_{up} (dashed) and W_{var} (solid) integration methods for “topped columns” (<20 dBZ) at (a),(b) 2229 and (c),(d) 2338 UTC. Error bars represent the mean difference between W_{up} and W_{var} .

illustrates the storm relative flow. The midlevel updraft is located at about $y = 5$ km. A small downdraft can be seen at $y = 11$ km. Vorticity rolls in the southern part of the storm can also be seen in regions where W_{var} was used. Continuity between the integration methodologies is relatively smooth, particularly at the low levels, but is a little more abrupt at near areas of strong reflectivity gradients. Anomalous winds associated with the W_{up} integration are also apparent in the upper levels, for example at $y = 8$ km (Figs. 8c,d).

The dual-Doppler derived updraft echo volume >5 m s⁻¹ (U5) starts at 2235 UTC (Fig. 9a). A threshold of 5 m s⁻¹ was applied in order to delineate areas of strong upward motion, consistent with where graupel production would be expected, with accompanying

electrification. The evolution of downdraft echo volume <-2 m s⁻¹ ($D2^2$) is also illustrated in Fig. 9a. Cell A has a much smaller U5 volume than cell B after the storm split at 2318 UTC, and is generally dominated by downdrafts (Fig. 9b). The U5 echo volume for cell A peaks at 2335 UTC, and has dissipated by 0000 UTC. Cell B continues to have a large U5 volume until 0000 UTC, with the peak occurring just after the split at 2320 UTC and a second peak at 2352 UTC. However, the second peak is coincident with the time of increased dual-Doppler

² The downdraft threshold was decreased compared to the updraft due in order to pick out low-level downdrafts, which as shown by Fig. 7, tend to have small magnitudes.

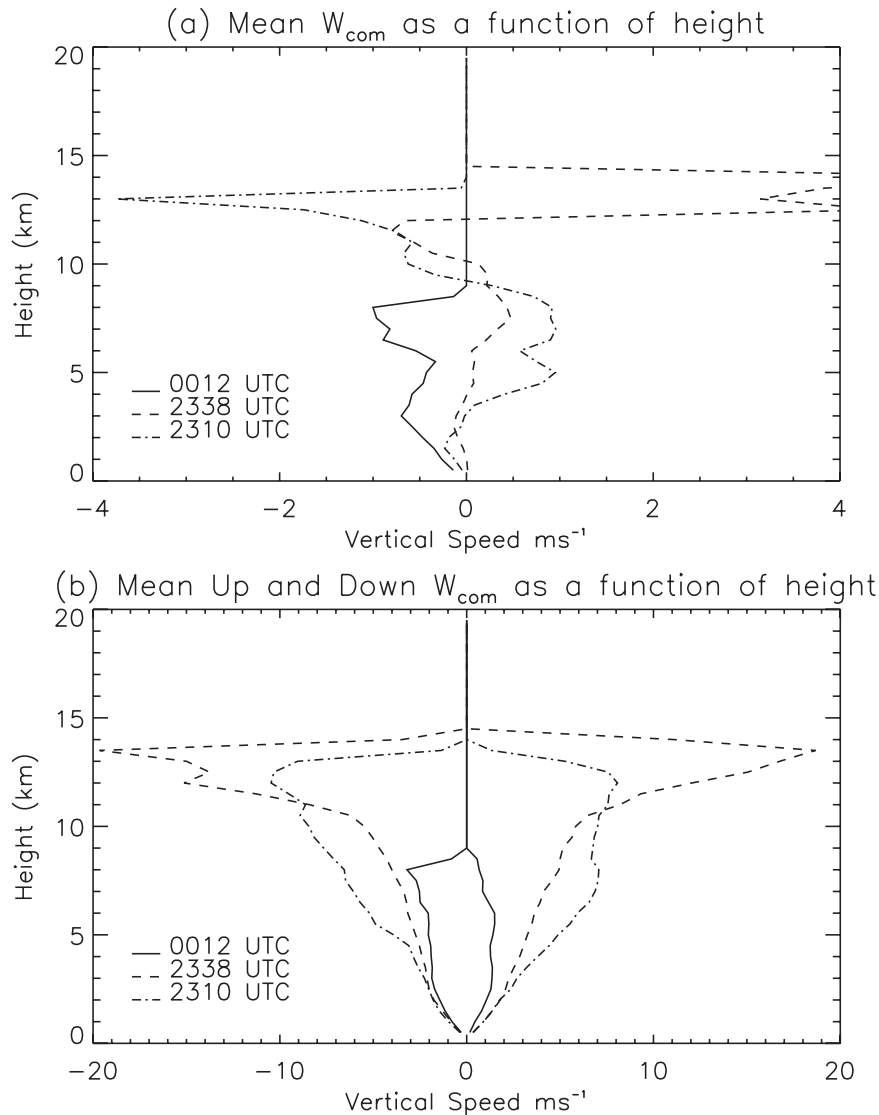


FIG. 7. Mean vertical wind using the W_{com} methodology (a) as a function of height, and (b) broken into up- and downward motion at three times during different stages of evolution.

coverage (Fig. 5b). The D2 volume peak is coincident with the U5 peak for cell B, as well as the several subsequent secondary peaks. For cell A, the U5 and D2 volumes have a raw correlation of 0.9, and a detrended (storm volume removed) lag correlation of 0.8 with U5 leading D2 by two time steps (6 min; Table 2). This would be consistent with formation of the updraft first, followed by development of the downdraft. Cell B U5 and D2 volumes have the highest correlation (0.6) at 0 lag (Table 2).

Perhaps a more enlightening illustration of the kinematic storm evolution is through time–height cross sections, allowing for the determination of the height–evolution of various features (Fig. 10). The total storm

complex U5 area shows two distinct peaks, one occurring at 2320 UTC between 5 and 8 km, and the other slightly higher at 7 and 9 km at 2333 UTC (Fig. 10a). By separating the cells into A and B (Figs. 10c,e), it is clear that the first large area of U5 is associated with cell B, while the higher second peak occurs in cell A, although cell B has a large area of U5 between the time of splitting (2318 UTC) and 2338 UTC. The total storm complex D2 time–height areas reveal a descending trend in the downdraft volume (Fig. 10b). The D2 area rapidly increases after the storm split, and a continuous area of large D2 area begins at 2335 UTC, and extends from the midlevels (9.5 km) down to the low levels (2 km). The D2 area reaches a maximum at 2347 UTC between 2 and 5 km,

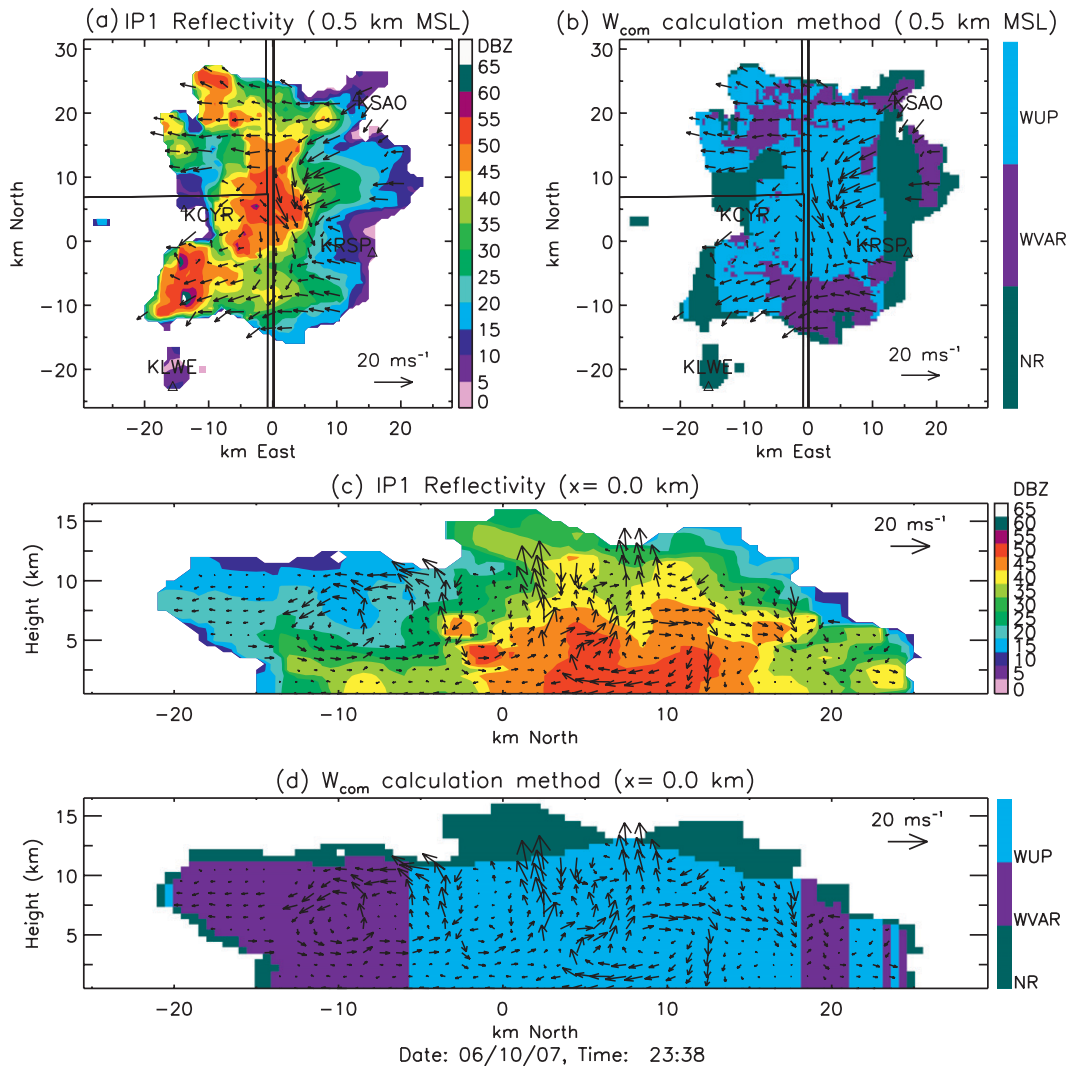


FIG. 8. (a),(b) Horizontal cross sections at 0.5 km MSL and (c),(d) vertical projections along $x = 0.0$, illustrated by the thick black line in (a) and (b) of IP1 data from 2338 UTC 10 Jun 2007. (a),(c) Mosaic reflectivity and (b),(d) the integration method used in the W_{com} methodology on a column-by-column basis. NR indicates “no retrieval” areas where there are reflectivity values but no winds could be calculated (e.g., along baselines and where only one radar was scanning). Winds shown are storm relative, where the mean storm motion has been subtracted.

about 15 min after the U5 peak in the midlevels. Cell A D2 area is centered higher (5 km) than the D2 area related to cell B, which peaks mostly below 5 km. The D2 peak for cell A is at 2340 UTC, just a few minutes after the cell A U5 peak. Cell B D2 reaches a maximum area at 2358 UTC, about 40 min after the U5 peak. As discussed previously, however, the dual-Doppler coverage was limited between 2245 and 2353 UTC, which could influence the locations and timing of the greatest updraft areas. However, the D2 threshold of < -2 m s⁻¹ biases the downdrafts to the mid- and low levels, which are still relatively well covered by dual-Doppler scanning during this time period.

As has been shown for this case, the IP1 dual-Doppler-derived wind fields provide valuable information about

the kinematic evolution and interactions occurring within a storm. The coordinated volume start times and targeted dual-Doppler scanning techniques reduce errors associated with storm advection, while the availability of more than two radars over parts of the network reduces the error variance, resulting in high-resolution, accurate, dual-Doppler-derived horizontal wind fields. Although the vertical wind magnitudes have been shown to be accurate to within 1–2 m s⁻¹ resulting from the integration method used, the series of up- and downdrafts illustrate the capability of IP1 to qualitatively observe both up- and downdrafts due to the low-level sampling and high temporal resolution, which aids in resolving these structures.

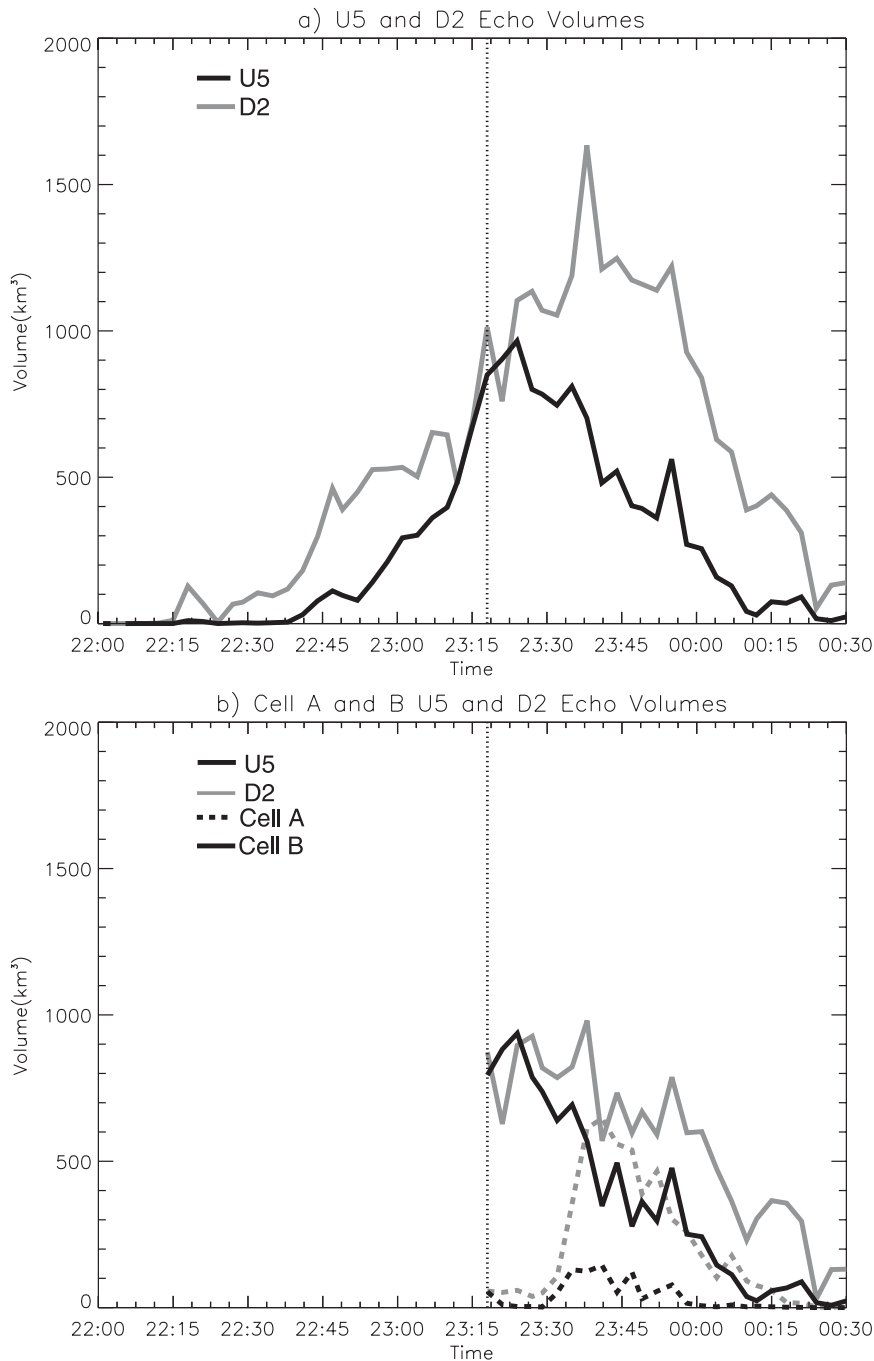


FIG. 9. Time series of updraft volume $>5 \text{ m s}^{-1}$ (black line) and downdraft volume $<-2 \text{ m s}^{-1}$ (gray line) for (a) the entire storm complex and (b) the contributions from cell A (dashed line) and cell B (solid line). The beginning of the storm split is marked with a dotted line (2318 UTC).

c. Microphysics

An altitude histogram of hydrometeor echo area derived from the IP1 and KOUN HID is illustrated in Fig. 11. Hydrometeors and their abbreviations used herein are

listed in Table 1. Although IP1 and KOUN data show similar trends in hydrometeor heights, KOUN clearly reveals a larger volume of ice crystals (CR and VI), as well as AG. This is a result of the reduced sensitivity of the IP1 radars relative to KOUN (Fig. 12), as well as

TABLE 2. Correlations among kinematic, microphysics, and lightning parameters. Values outside the parentheses are raw correlations at zero lag, while values inside the parentheses represent the best detrended lag correlations (the storm volume identified by each radar, respectively, was removed from both x and y), with the lag values indicated after the @ symbol and representing one radar scan interval. For example, a lag of 1 for IP1 data represents 3 min, while for KOUN data a lag of 1 corresponds to 5 min. Positive lag values correspond to y leading x .

x	y	Storm complex IP1	Storm complex KOUN	Cell A IP1	Cell A KOUN	Cell B IP1	Cell B KOUN
D2	U5	0.8 (−0.4 @ −3)	—	0.9 (0.8 @ 2)	—	0.9 (0.6 @ 0)	—
LDG	HDG	0.9 (0.6 @ 1)	0.7 (0.9 @ 3)	0.9 (0.8 @ 1)	0.97 (0.95 @ 0)	0.98 (0.8 @ 0)	0.98 (0.9 @ 0)
U5	Graupel	0.9 (0.8 @ −1)	—	0.9 (0.8 @ 0)	—	0.9 (0.8 @ 0)	—
D2	Graupel	0.9 (−0.3 @ −5)	—	0.9 (0.8 @ 1)	—	0.9 (−0.3 @ 2)	—
IC	VI	0.5 (−0.3 @ 1)	0.9 (0.8 @ −2)	0.01 (−0.4 @ 0)	0.1 (−0.7 @ −1)	0.4 (−0.4 @ 1)	0.8 (−0.6 @ 2)
TFR	Graupel	0.6 (−0.4 @ −5)	0.6 (0.6 @ −1)	0.5 (0.7 @ −3)	0.7 (0.9 @ −1)	0.5 (−0.6 @ 0)	0.9 (−0.4 @ 1)
CG	IC	0.8 (0.6 @ 0)	0.9 (0.8 @ 0)	0.8 (0.8 @ 0)	0.9 (0.9 @ 0)	0.7 (0.7 @ −2)	0.9 (0.6 @ 1)

reduced upper-level coverage by IP1 (Fig. 5a). Both radar volumes show a peak in CR at 9 km. The lower coverage of IP1 allows it to detect RN and DZ very near the surface, while KOUN tapers off significantly below 2.5 km because of the range from KOUN to the echoes (Fig. 11a). Interestingly, LDG and HDG volumes between the two radars are strikingly similar (Fig. 11b). IP1 shows AG peaking at 4.5 km, the same height of the melting layer, while KOUN indicates the AG peak much higher, around 7 km. The subtle differences between HDG and LDG (not discussed) and the more significant differences in AG could be a function of the coarser vertical resolution of the KOUN data. The general trends indicate the potential for better observations of the low to midlevels with IP1 compared to longer wavelength radars when operating at longer ranges, and illustrates that possible non-Rayleigh scattering effects do not significantly inhibit bulk hydrometeor classifications.

The microphysical evolution of the storm can be inferred by employing the HID to look at the formation of different types of hydrometeors throughout the lifetime of the storm complex. The KOUN VI volume increases rapidly at 2307 UTC, and reaches an absolute maximum at 2339 UTC (Fig. 13a). IP1 generally captures much less VI volume because of coverage and sensitivity. The IP1 VI volume peaks approximately every 20 min beginning at 2307 UTC and ending at 2345 UTC (Fig. 13a), a trend not indicated by KOUN and possibly an artifact of upper-level coverage. IP1 VI volumes for cell A and B both peak at 2345 UTC, while KOUN VI for cell B peaks much earlier at 2325 UTC (Fig. 13b). Both IP1 and KOUN do not show significant volumes of VI associated with cell A until 2338 UTC, which is consistent with the peak in U5 area for cell A (Fig. 10). If we assume that the height of the 40-dBZ echo can be used as a measure of the intensity of a storm, KOUN 40-dBZ echo heights start at 8.5 km and increase to about 14 km by 2325 UTC (Fig. 13c). IP1 sees a similar trend. Both IP1 and KOUN show that the 40-dBZ height for

cell A is slightly lower than storm B after the split, and rapidly falls to 4 km by 0000 UTC, while cell B heights remain greater than 12 km until 0030 UTC 11 June when the storm exits the IP1 network (Fig. 13d).

For simplicity, HDG and LDG have been combined into a single category termed “graupel.” Time–height contours of graupel echo area derived from the HID analysis are shown in Fig. 14. General trends observed by IP1 show a rapid onset of graupel volume beginning at 2237 UTC. KOUN graupel trends are smoother, indicate the presence of graupel sooner than IP1, and reach a maximum at 2322 UTC. The difference in the onset of graupel is likely a result of the reduced coverage above 3 km by IP1 during the early times of the storm (Fig. 5a). KOUN and IP1 graupel areas show similar trends, with two relative maxima at 8 km and between 5 and 6 km that are associated with the two types of graupel (Figs. 14a,b). Separate analysis confirms that the upper maximum at 8 km is LDG, while the lower maximum is related to HDG. The maximum area of KOUN LDG occurs at 2333 UTC, while the IP1 LDG peak occurs 4 min later at 2337 UTC. The KOUN HDG maximum is smaller than the KOUN LDG and occurs at the same time as the peak in LDG. The HDG maximum area identified by IP1 is larger than the peak in LDG and occurs 7 min later at 2345 UTC. However, as noted previously, the relative IP1 coverage above 5-km peaks at this time and may cause the increased area. In comparing cell A and cell B, it is clear that cell B dominates the overall storm trend, with two distinct layers associated with LDG and HDG. Both KOUN and IP1 have high correlations between LDG and HDG, with HDG leading LDG by anywhere from zero to three time steps (Table 2). Correlations between the two are improved by examining individual cells (Table 2).

The U5 echo area peaked between 6 and 8 km (Fig. 10), and the LDG echo area is greatest toward the top of this layer (8–9 km; Fig. 14). In fact, U5 and graupel are highly correlated for both cells and the storm complex, with a tendency for U5 to lead the graupel volumes by one

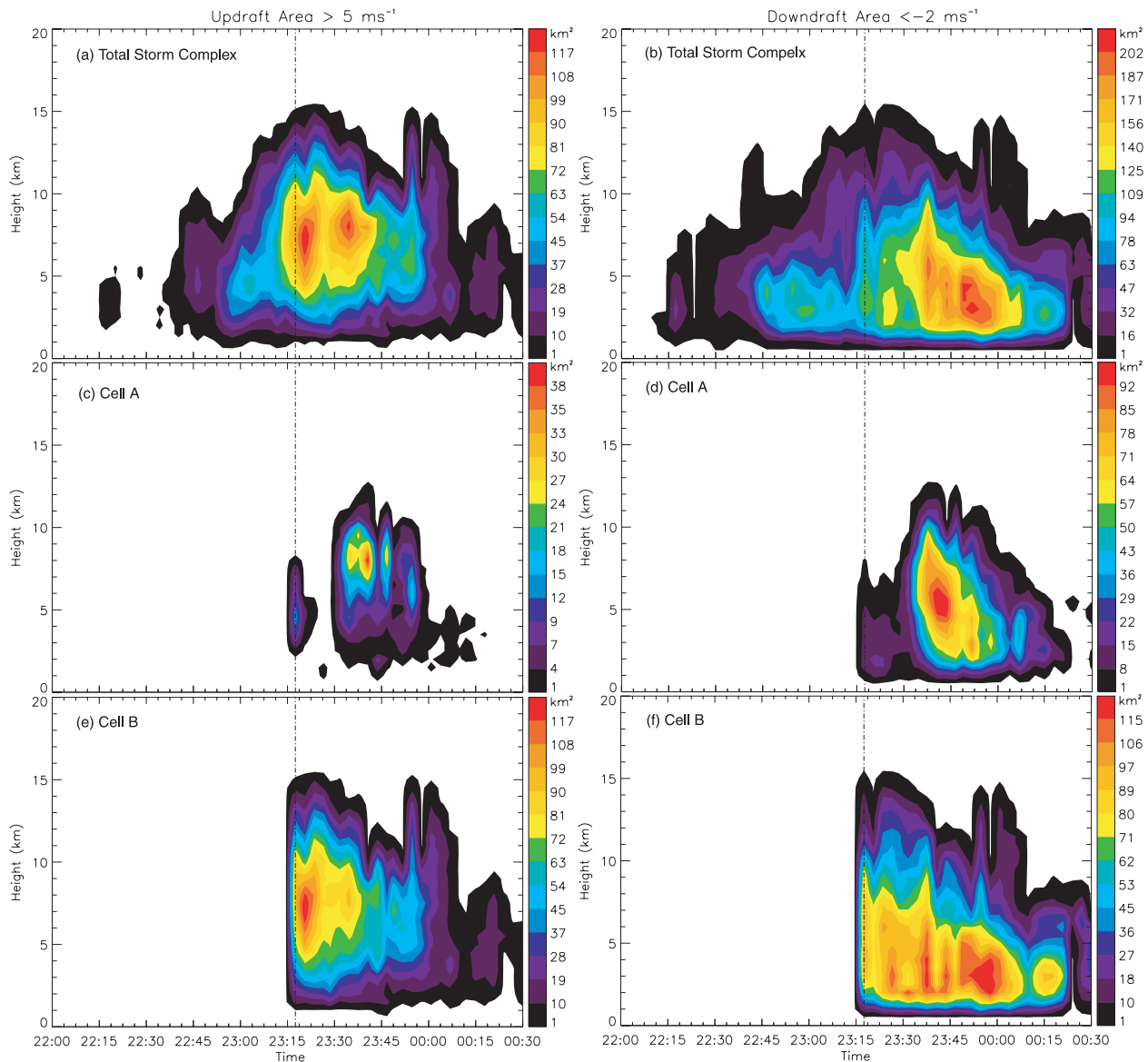


FIG. 10. Time–height cross section of (left) updraft area $>5 \text{ m s}^{-1}$ and (right) downdraft area $<-2 \text{ m s}^{-1}$ for (top) the storm complex, (center) cell A, and (bottom) cell B. The beginning of the split into cell A and B is indicated with the dash–dot line.

time step (3 min), which supports the theory of the updraft strengthening and lofting graupel into the upper levels of the storm (Table 2). The detrended correlation for cell A shows a strong lag correlation (0.8) with graupel leading the downdraft by one time step (3 min; Table 2). The correlation for cell B is weaker and negative (meaning D2 volume reaches a maximum as graupel reaches a minimum), but still with graupel leading D2 by several minutes (Table 2). The peak in graupel area occurs from 2335 to 2347 UTC, while the D2 area reaches a max area 6 min later at 2352 UTC.

Qualitative examples of the combined microphysics and kinematics are illustrated in Fig. 15. The storm-relative

winds derived from the dual-Doppler synthesis have been overlaid on IP1 observations (Figs. 15a,c,d). The HID categorizations are shown, but the RN and DZ categories below 2.5 km have been broken into four categories based on the blended algorithm rain-rate calculations. The four rain categories are light rain (LTRN; $<2.5 \text{ mm h}^{-1}$), moderate-light rain (MLTRN; $2.5\text{--}25 \text{ mm h}^{-1}$), moderate-heavy rain (MHVYRN; $25\text{--}50 \text{ mm h}^{-1}$), and heavy rain (HVVYRN; $>50 \text{ mm h}^{-1}$).

Figure 15 shows horizontal and vertical cross sections of data at 2321 UTC, just as the linear-organized storm began to split into cell A and cell B. Storm-relative surface flow is from the northeast (Fig. 15a). As the air

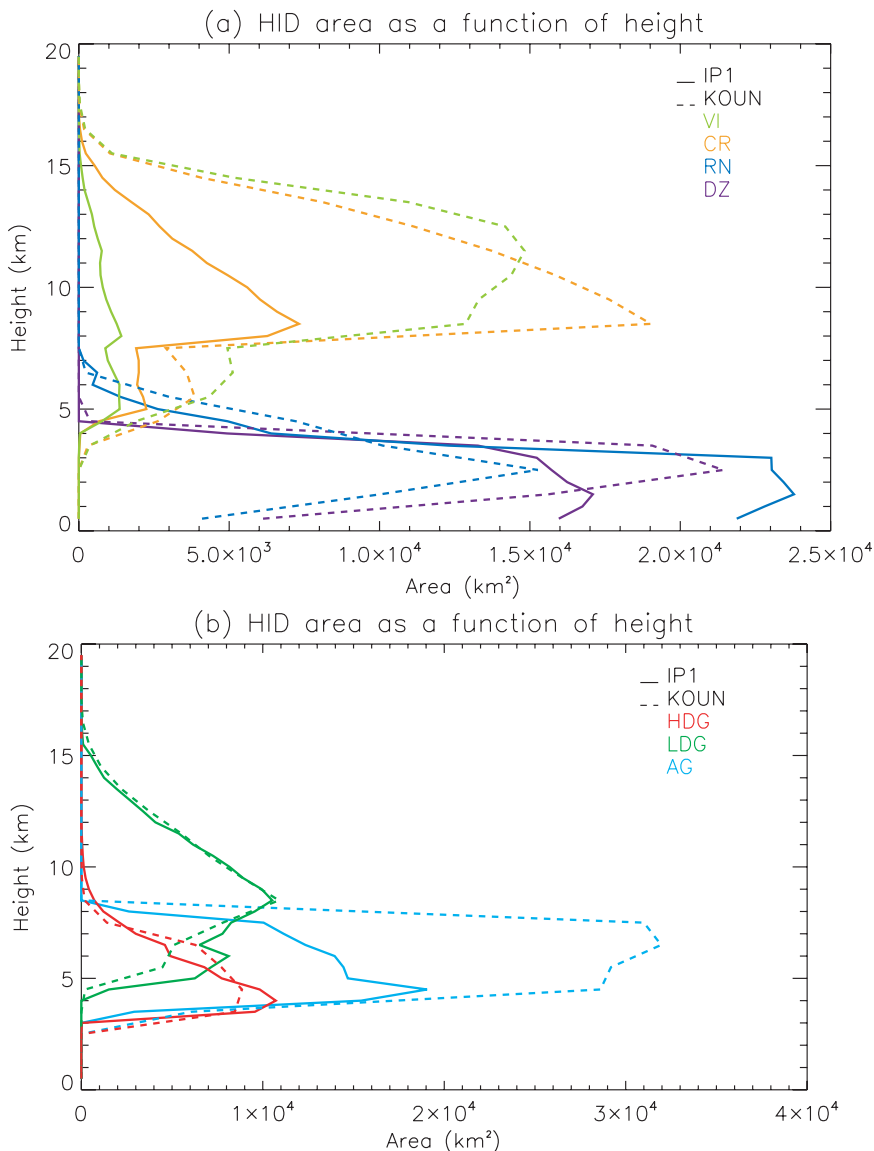


FIG. 11. HID area for different hydrometeors as identified by IP1 (solid) and KOUN (dashed) during the entire storm lifetime. See Table 1 for HID classification types and abbreviations.

enters the leading edge of the storm, some of it begins to lift, forming new cells (Fig. 15c). The main updraft is located above 5 km at 30-km range along the vertical cross section, which is along the direction of propagation. This region of strong upward motion is characterized by large areas of HDG and LDG, as well as RN identified above the melting layer (likely supercooled liquid water). Behind the main updraft, the motions are weaker, mostly characterized by downward motion below 3.5 km and upward motion above 5 km. Surface rain rates are largest ($>50 \text{ mm h}^{-1}$) to the southwest of the main updraft, and are coincident with relatively strong downward motion. KOUN cross sections from four

minutes earlier demonstrate two main reflectivity cores (Fig. 15e), which are not as distinct in the IP1 data. General HID trends are similar between the two wavelengths (Figs. 15d,f), with IP1 providing details of smaller-scale features. However, KOUN identifies large regions of VI along the upper-level edges of the storm that are not seen by IP1.

These qualitative observations support some of the quantitative findings described above, and illustrate some of the advantages and disadvantages of the IP1 radar network. For example, the coverage area and artifacts from the mosaicking and W_{com} procedures are apparent, but the increased spatial and temporal resolution

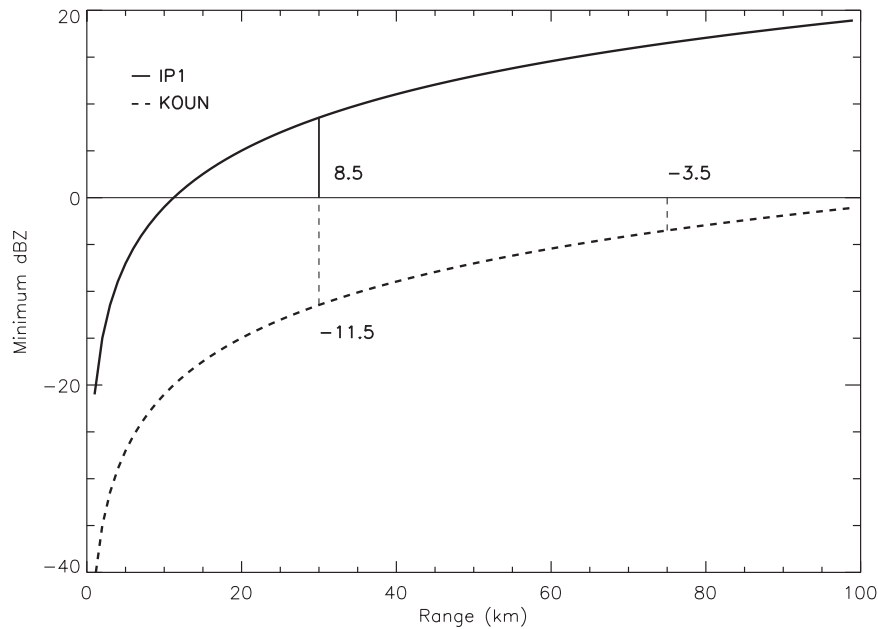


FIG. 12. Comparison of radar sensitivity for IP1 (solid line) and KOUN (dashed line). The sensitivity at the IP1 maximum range (30 km) and at the approximate distance of IP1 from KOUN (75 km) is indicated.

compared to KOUN in this case is also notable. Broad features in the KOUN data, such as the rain core above 5 km along the 27 km slant path (Fig. 15f), are more localized and defined in the IP1 data (Fig. 15d). Rain features at the lowest altitude are also more concentrated in the IP1 data (Fig. 15a) compared to widespread areas of heavy rain identified by KOUN (Fig. 15b). Height plots of HDG area indicate that IP1 detects approximately the same amount of HDG and LDG as KOUN, and at approximately the same height (Fig. 11). This is important for studies involving interactions with lightning, although IP1 has degraded coverage of the ice crystals in the upper levels of the storm, which are critical to the charging processes. The low-level coverage of IP1 also samples near-surface divergence that helps resolve low-level downdrafts and improve vertical wind retrievals, as well as observe precipitation near the surface that cannot be seen by KOUN at longer ranges.

d. Lightning

Thunderstorms have been shown to often have a dipole or tripole charge structure (Williams 1989, 2001). A so-called normal dipole generally exhibits negative charge near -10°C , with the positive charge residing above the negative, above approximately -30°C (Williams 1985; Williams et al. 1994). A “normal tripole” has a smaller region of positive charge near the 0°C isotherm (Williams 1989). This type of charge structure is thought to be the

result of noninductive ice–ice collision mechanisms, whereby collisions between graupel and ice crystals falling with differential velocities transfer charge. The amount of charge and polarity transferred between particles is dependant on the riming rate, liquid water content, and temperature at which the collisions occur (Takahashi 1978; Saunders and Peck 1998; Berdeklis and List 2001). In a normal dipole, graupel generally acquires negative charge and ice crystals positive charge. In this case the graupel particle is growing by riming and its surface is in a sublimational state with respect to vapor transfer (Williams et al. 1991, 1994). We place the IP1 observations in the context of this model using the lightning observations (Fig. 16).

Using the LMA for charge analysis, it was clear that this storm exhibited normal polarity with two distinct regions of charge: midlevel negative charge and upper-level positive charge (Figs. 16a,b). Pockets of lower positive charge below the negative source region were also observed, providing the source region for negative cloud-to-ground flashes. Temperature data from the 1200 UTC OUN sounding indicate that the negative source region resides between -10° and -25°C with the positive region above the negative, which is consistent with the normal dipole storm structure (Fig. 16; Williams 2001).

The NLDN detected 333 ground strikes, while the LMA identified upward of 4000 total flashes. The IC component accounted for 92% of the total lightning. The three-minute (corresponding to the IP1 scan interval)

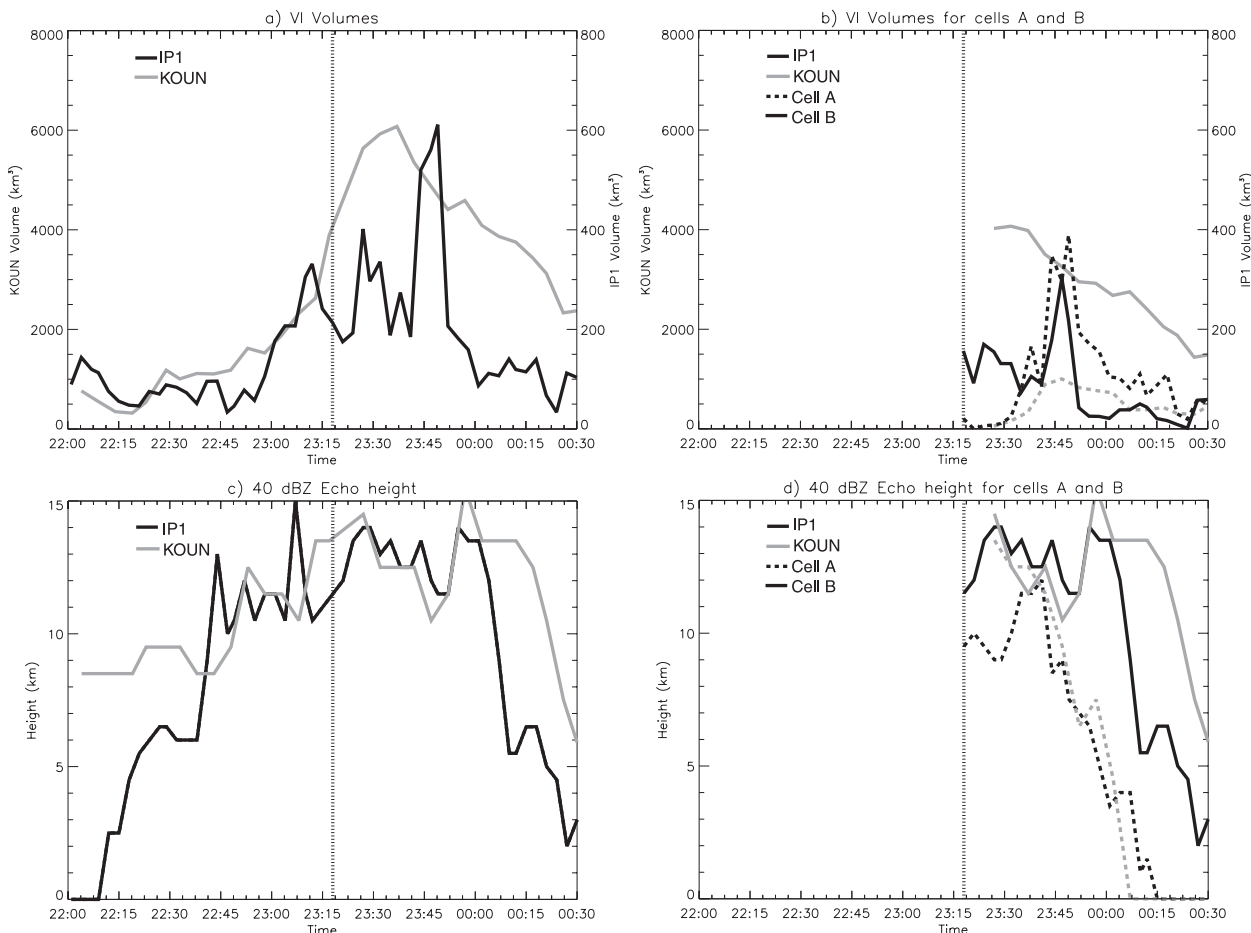


FIG. 13. Time series of IP1 (black) and KOUN (gray) VI echo volumes (a) for the storm complex and (b) broken into cell A (dashed line) and cell B (solid line) and for the 40-dBZ echo-top heights for (c) the entire storm and (d) contributions from cell A (dashed line) and cell B (solid line). The beginning of the storm split is marked with a vertical black line.

total lightning flash rate (TFR) time series exhibits a trimodal trend, dominated by the intracloud flash rate (Fig. 16c). The three peaks occur at 2307, 2322, and 0010 UTC with the largest peak at 2322 UTC. IC lightning onset begins at 2222 UTC, and markedly increases at 2245 UTC. The CG flash rate starts nearly a half an hour after the IC at 2250 UTC, although only five minutes after the rapid increase of IC at 2245 UTC. The onset of IC prior to the beginning of CG flashes is a general trend in storm electrification noted by many authors (e.g., Carey and Rutledge 1996; Goodman et al. 1988; Williams et al. 1989). Two minimums in TFR occur at 2315 and 2348 UTC. While both cell A and B are clearly dominated by IC flashes, cell A had nearly twice the percentage of CG flashes (13%) compared to cell B (7%).

Graupel echo area contours overlaid on the LMA source density reveal the negative source regions are generally associated with the largest area of graupel as identified by both IP1 and KOUN (Figs. 16a,b). Graupel

area maxima lead peaks in IC flash rate (Fig. 16), similar to findings of Carey and Rutledge (1996). The highest correlations occur when graupel leads the TFR (which is dominated by IC) by 5 to 15 min. (Table 2). The KOUN ice echo area (VI and CR) shows the positive source region containing the greatest area of ice crystals (Fig. 16b), an observation consistent with several of the noninductive charging mechanism studies (Takahashi 1978; Saunders and Peck 1998).

The peak in IP1 VI volume at 2345 UTC (Fig. 13a) corresponds to the minima in the IC flash rate, which is consistent with an increasing local electric field, aligning ice crystals in the vertical. It is difficult to say if this is the case since negative correlations between IP1 VI volume and IC are low (−0.3 to −0.4) with lag of one (Table 2). Although the same “pulsing” is not obvious in the KOUN time series, correlations are mixed, with negative values for individual cells but a high positive correlation for the overall storm complex (0.8). Lags range from VI

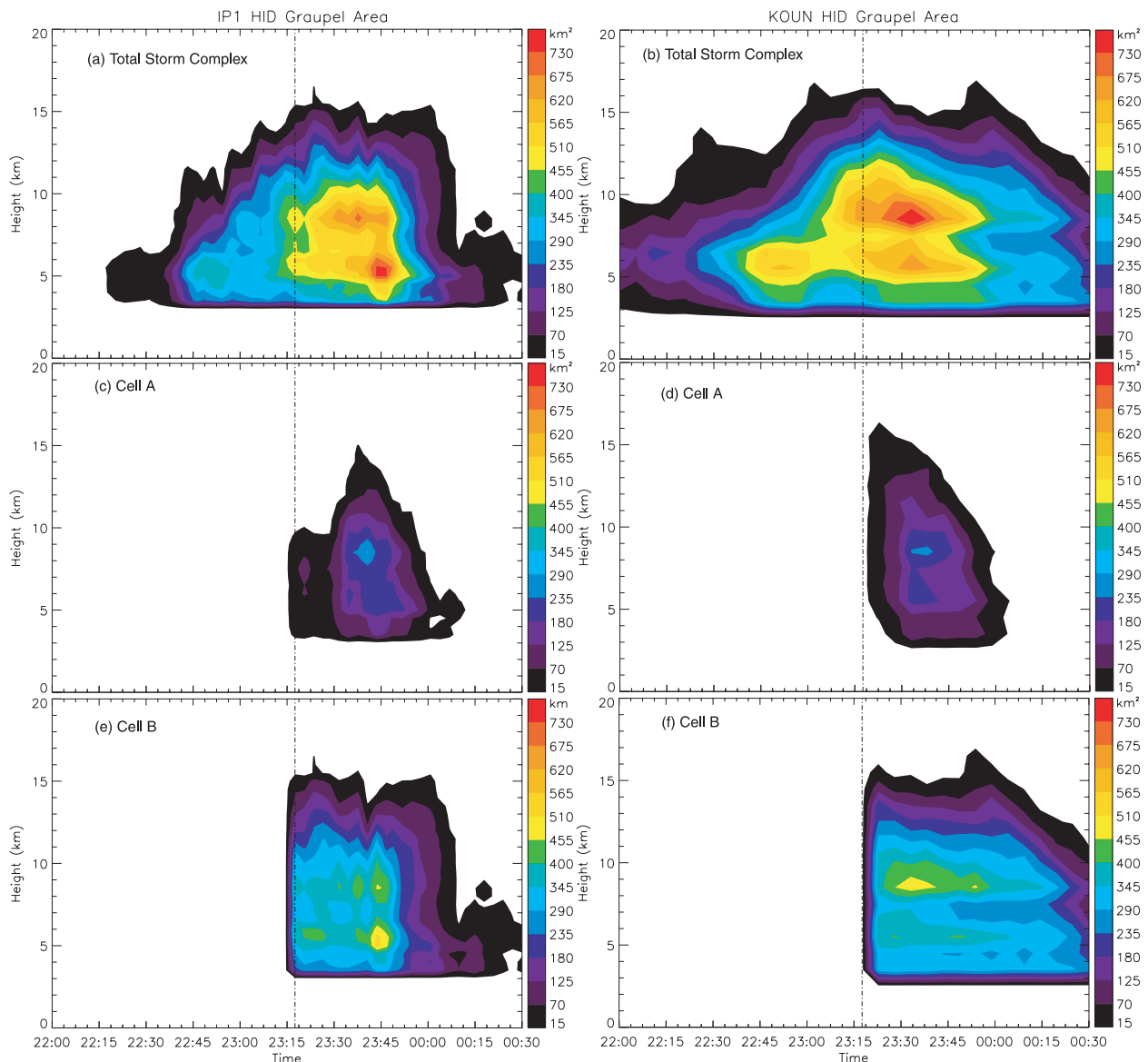


FIG. 14. Time–height cross section of graupel area for (left) IP1 and (right) KOUN for (top) the storm complex, (middle) cell A, and (bottom) cell B. The beginning of the storm split is marked with a dash-dot line.

leading by 10 min in cell B to IC leading by 10 min for the storm complex (Table 2). It is interesting to note that the mean heights associated with VI as identified by KOUN are centered between 10 and 13 km (Fig. 11a), the same region as the highest density of OK-LMA sources, which is not as apparent in IP1 data because of the previously discussed sensitivity and coverage.

4. Discussion

The unique network of X-band polarimetric adaptively scanning radars employed by CASA IP1 was used to examine storm dynamics and kinematics on a convective

scale. Although dual-Doppler areas were targeted using the unique DCAS system, insufficient coverage of the upper levels dictated integration methods including upward integration techniques to retrieve the 3D wind. This was coupled with W_{var} when echoes were topped in order to balance anomalous winds resulting from upward integration with inadequate coverage of the upper boundary condition. It was illustrated that this methodology resulted in the same general trends as using completely topped columns, but with large magnitude errors ($1\text{--}2\text{ m s}^{-1}$), particularly in the upper levels ($>8\text{ km}$). Thus, analysis focused on nonmagnitude-related metrics. The low-level coverage of IP1 is important for

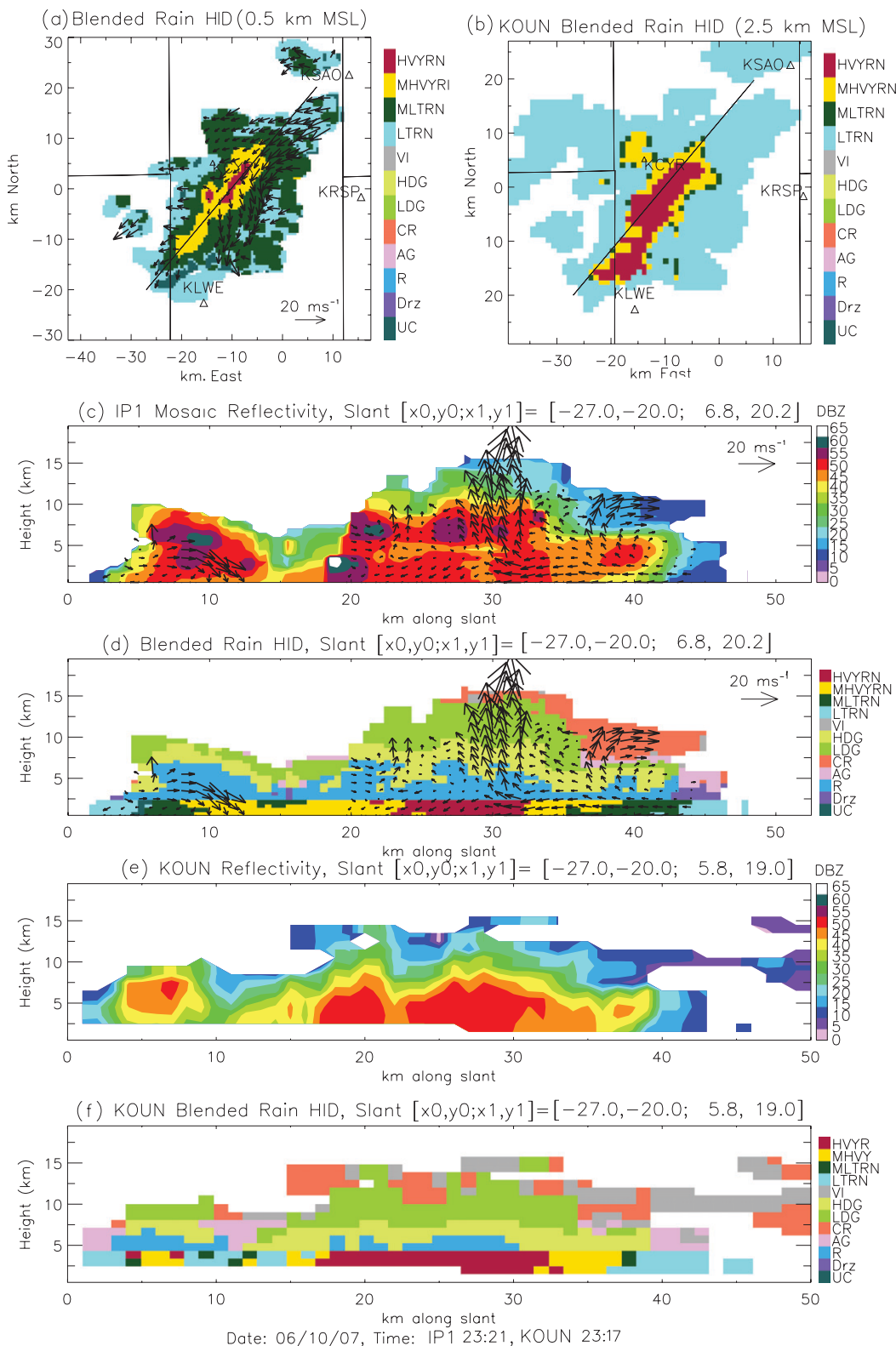


FIG. 15. Microphysical and kinematic observations at (a),(c),(d) 2321 UTC by IP1 and (a),(e),(f) 2317 UTC by KOUN. The expanded HID analysis utilizing the X-band blended rain algorithm to determine surface rain rates below 2.5 km is illustrated in (a) and (d), and the expanded KOUN HID rain is shown for comparison in (b) and (f). The vertical cross sections (c),(d),(e),(f) were taken along the direction of propagation, as illustrated by the line in (a) and (b). Vectors are storm-relative winds derived from dual-Doppler analysis.

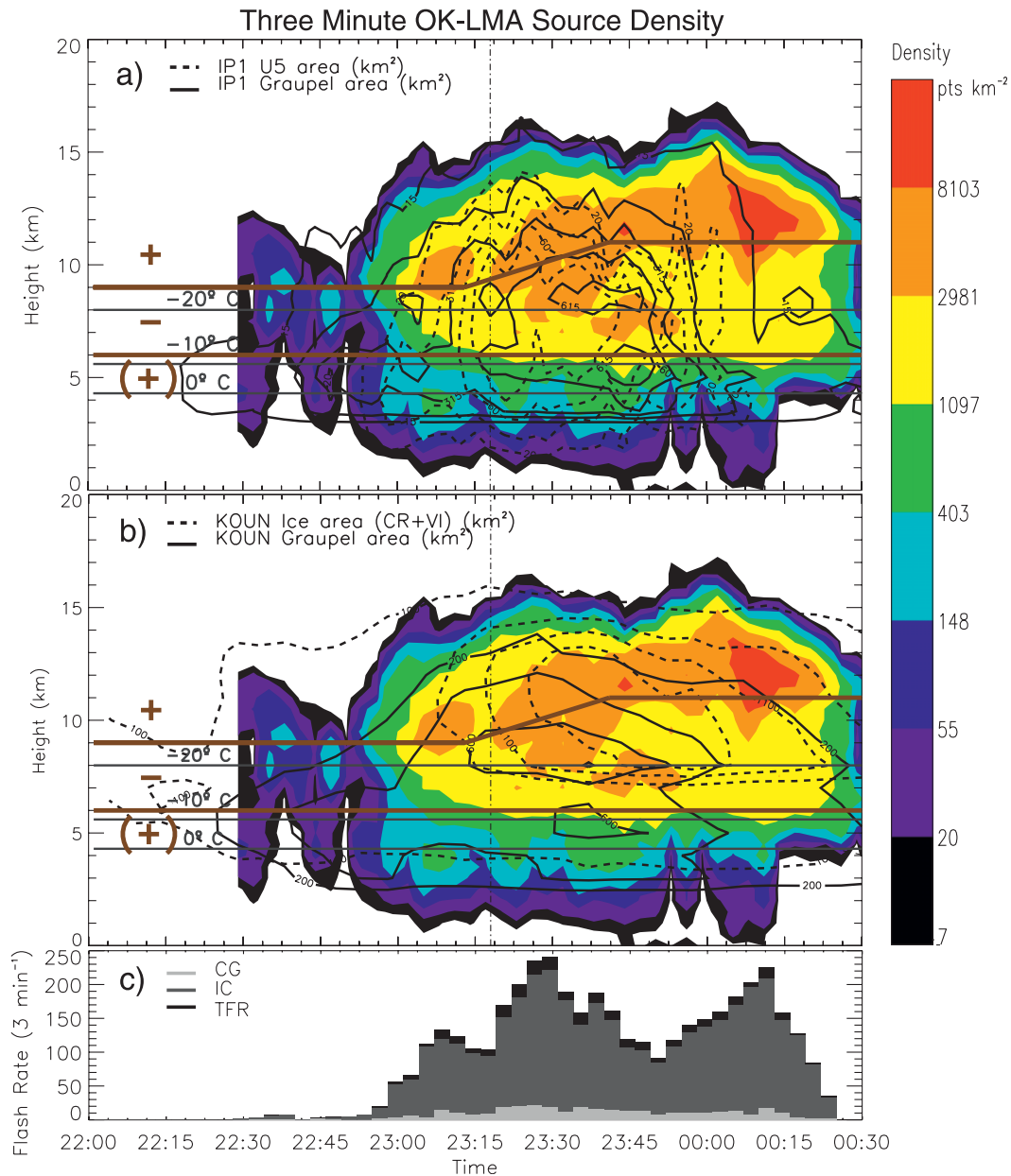


FIG. 16. Time–height contours of 3-min OK-LMA VHF source density with contours of (a) IP1 updraft area $>5 \text{ m s}^{-1}$ (dashed black line) and graupel area (solid black line) and (b) KOUN ice crystal area (dashed black line) and graupel (solid black line). The inferred charge layers are indicated in brown and the temperature from the 1200 UTC 10 Jun 2007 sounding is denoted in dark gray. (c) Depicts 3-min lightning flash rates for TFR (black), IC (dark gray), and CG (light gray).

dual-Doppler retrievals in that it provides a better initial condition for the upward integration technique, and allows for detection of divergence often associated with low-level downdrafts. These types of observations could help detect downbursts in future cases (Wilson et al. 1984), as well as strong areas of outflow.

IP1 observations of the storm complex evolution loosely follow that described in Carey and Rutledge

(1996) and Williams et al. (1989) where the updraft develops, leading to graupel formation several minutes later, followed by the onset of IC lightning shortly thereafter (Fig. 16). The IC flash rates quickly increase as the graupel and updraft volumes increase. CG flashes begin once HDG is present in the 5–7-km heights (Williams et al. 1989). As more graupel is suspended in the midlevels by the updraft, the downdraft starts to

form, bringing precipitation to the surface. Although IC flash rates in this case resurge as the storm is dissipating, CG flash rates cease as the graupel volume drops off. IP1 data did show significant correlations between graupel and U5, as well as graupel and TFR. It should be noted that multicellular storms could inherently have weak correlations because of the different cells in different phases of storm lifetime. The IP1 network also allowed for kinematic comparisons with lightning and graupel formation, highlighting the evolution of the updraft relative to the development of the upper-level microphysics and subsequent charging leading to electrification. Many of these observations were corroborated by KOUN, although kinematic analysis was not available. The better spatial resolution of IP1 also allowed finer time–height contouring compared to the coarser resolution of KOUN, although this is a result of the arrangement of the radars and not necessarily indicative of general IP1 advantages.

One significant drawback of the IP1 radars revealed in this study was the lack of consistent coverage by the radars. The adaptive scanning strategy is an important aspect of balancing high temporal resolution, resources in the network, and total coverage area of the networked radars. However, inconsistent storm coverage results in ambiguities regarding real fluctuations in storm parameters versus changes in the scanning strategy, making quantitative analysis difficult. The lack of coverage in the upper levels reduces the overall storm coverage and decreases the understanding of ice-phase processes that are important for lightning and electrification. The lack of upper-level coverage also limits the quality of the dual-Doppler derived vertical winds, impacting the quantitative analysis of up- and downdraft dynamics.

Despite the lack of consistent upper-level coverage, the low-level coverage provided by the IP1 radars has significant benefits for rainfall estimation, melting layer and surface dynamics. Comparisons with KOUN showed that the IP1 coverage was enough to accurately identify graupel areas in the midlevels, which have an influence on the downdraft development, electrification, and rain processes. The near-surface velocity sampling helps to restrain errors in estimating the vertical wind, particularly when W_{up} is necessitated. Comparisons with lightning sensors showed that kinematic and microphysical observations were consistent with current charging theories. Application of the analysis techniques to the 10 June 2007 case demonstrates the potential for convective scale studies using a network of X-band polarimetric radars such as IP1.

Future studies should continue to evaluate the potential for IP1 to improve understanding of storm evolution

and interactions. Other types of storms, such as isolated cells, super cells, squall lines, and frontal passages should be analyzed. In particular, winter season storms, which, because of their generally lower cloud tops and subdued kinematics, could be ideal for study by the IP1 network. Validation of both the microphysics and the kinematics with other sensors, such as profilers and disdrometers, needs to be performed.

Acknowledgments. The authors would like to extend appreciation to Dr. Chandrasekar at CSU for his assistance in obtaining and interpreting CASA IP1 data. Dr. S. Lim of CSU provided the network-based attenuation corrected data for analysis; Dr. Y. Wang of CSU developed the scanning strategy to optimize multiple-Doppler analysis. Dr. Terry Schuur of OU and Dr. Don MacGorman of NSSL graciously provided the KOUN and OK-LMA, respectively. The authors would also like to thank Dr. Timothy Lang and Dr. Rob Cifelli for helpful and insightful discussion. This work is supported primarily by the Engineering Research Centers Program of the National Science Foundation under NSF Award 0313747, Colorado State University, and University of Massachusetts Contract UM04-002341.

REFERENCES

- Berdeklis, P., and R. List, 2001: The ice crystal–graupel charging mechanism of thunderstorm electrification. *J. Atmos. Sci.*, **58**, 2751–2770.
- Bohne, A. R., and R. C. Srivastava, 1976: Random errors in wind and precipitation fall speed measurement by a triple Doppler radar system. Preprints, *17th Radar Meteorology Conf.*, Seattle, WA, Amer. Meteor. Soc., 7–14.
- Bringi, V. N., and V. Chandrasekar, 2001: *Polarimetric Doppler Weather Radar: Principles and Applications*. Cambridge University Press, 636 pp.
- Carey, L. D., and S. A. Rutledge, 1996: A multiparameter radar case study of the microphysical and kinematic evolution of lightning producing storm. *Meteor. Atmos. Phys.*, **59**, 33–64.
- Chandrasekar, V., and S. Lim, 2008: Retrieval of reflectivity in a networked radar environment. *J. Atmos. Oceanic Technol.*, **25**, 1755–1767.
- Cifelli, R., W. A. Petersen, L. D. Carey, S. A. Rutledge, and M. A. F. da Silva Dias, 2002: Radar observations of the kinematic, microphysical, and precipitation characteristics of two MCSs in TRMM LBA. *J. Geophys. Res.*, **107**, 8077, doi:10.1029/2000JD000264.
- Cummins, K. L., M. J. Murphy, E. A. Bardo, W. L. Hiscox, R. B. Pyle, and A. E. Pifer, 1998: A combined TOA/MDF technology upgrade of the U. S. National Lightning Detection Network. *J. Geophys. Res.*, **103D**, 9035–9044.
- Dolan, B., and S. A. Rutledge, 2009: A theory-based hydrometeor identification algorithm for X-band polarimetric radars. *J. Atmos. Oceanic Technol.*, **26**, 2071–2088.
- Doviak, R. J., P. S. Ray, R. G. Strauch, and L. J. Miller, 1976: Error estimation in wind fields derived from dual-Doppler radar measurement. *J. Appl. Meteor.*, **15**, 868–878.

- Fulton, R. A., J. P. Breidenbach, D. J. Seo, D. A. Miller, and T. O'Bannon, 1998: The WSR-88D rainfall algorithm. *Wea. Forecasting*, **13**, 377–395.
- Goodman, S. J., D. E. Buechler, P. D. Wright, and W. D. Rust, 1988: Lightning and precipitation history of a microburst producing storm. *Geophys. Res. Lett.*, **15**, 1185–1188.
- Gorgucci, E., V. Chandrasekar, and L. Baldini, 2006: Correction of X-band radar observation for propagation effects based on the self-consistency principle. *J. Atmos. Oceanic Technol.*, **23**, 1668–1681.
- Kasemir, H. W., 1960: A contribution to the electrostatic theory of lightning discharge. *J. Geophys. Res.*, **65**, 1873–1878.
- Kessinger, C. J., P. S. Ray, and C. E. Hane, 1987: Oklahoma squally line of 19 May 1977. Part I: A multiple Doppler analysis of convective and stratiform structure. *J. Atmos. Sci.*, **44**, 2840–2864.
- Mansell, E. R., D. R. MacGorman, C. L. Ziegler, and J. M. Straka, 2002: Simulated three-dimensional branched lightning in a numerical thunderstorm model. *J. Geophys. Res.*, **107**, 4052, doi:10.1029/2000JD000024.
- Matejka, T., and D. L. Bartels, 1998: The accuracy of vertical air velocities from Doppler radar data. *Mon. Wea. Rev.*, **126**, 92–117.
- Matrosov, S. Y., K. A. Clark, B. E. Martner, and A. Tokay, 2002: X-band polarimetric radar measurements of rainfall. *J. Appl. Meteor.*, **41**, 941–952.
- , R. Cifelli, P. C. Kennedy, S. W. Nesbitt, S. A. Rutledge, V. N. Bringi, and B. E. Martner, 2006: A comparative study of rainfall retrievals based on specific differential phase shifts at X- and S-band radar frequencies. *J. Atmos. Oceanic Technol.*, **23**, 952–963.
- McLaughlin, D., and Coauthors, 2009: Short-wavelength technology and the potential for distributed networks of small radar systems. *Bull. Amer. Meteor. Soc.*, **90**, 1797–1817.
- Mohr, C. G., and L. J. Miller, 1983: CEDRIC—A software package for Cartesian space editing, synthesis and display of radar fields under interactive control. Preprints, *21st Conf. on Radar Meteorology*, Boston, MA, Amer. Meteor. Soc., 569–574.
- Nelson, S. P., and R. A. Brown, 1987: Error sources and accuracy of vertical velocities computed from multiple-Doppler radar measurements in deep convective storms. *J. Atmos. Oceanic Technol.*, **4**, 233–238.
- O'Brien, J. J., 1970: Alternative solutions to the classical vertical velocity problem. *J. Appl. Meteor.*, **9**, 197–203.
- Park, S.-G., V. N. Bringi, V. Chandrasekar, M. Maki, and K. Iwanami, 2005: Correction of radar reflectivity and differential reflectivity for rain attenuation at x band. Part I: Theoretical and empirical basis. *J. Atmos. Oceanic Technol.*, **22**, 1621–1632.
- Ray, P. S., C. L. Ziegler, W. Bumgarner, and R. J. Serafin, 1980: Single- and multiple-Doppler radar observations of tornadic storms. *Mon. Wea. Rev.*, **108**, 1607–1625.
- Rison, W., R. J. Thomas, P. R. Krehbiel, T. Hamlin, and J. Harlin, 1999: A GPS-based three-dimensional lightning mapping system: Initial observations in central New Mexico. *Geophys. Res. Lett.*, **26**, 3573–3576.
- Rust, W. D., and Coauthors, 2005: Inverted-polarity electrical structures in thunderstorms in the Severe Thunderstorm Electrification and Precipitation Study (STEPS). *Atmos. Res.*, **76**, 247–271.
- Ryzhkov, A., and D. S. Zrnica, 1998: Discrimination between rain and snow with a polarimetric radar. *J. Appl. Meteor.*, **37**, 1228–1240.
- , S. E. Giangrande, and T. J. Schuur, 2003: Rainfall measurements with the polarimetric WSR-88D radar. National Severe Storms Laboratory Rep., 98 pp.
- , T. J. Schuur, D. W. Burgess, P. L. Heinselman, S. E. Giangrande, and D. S. Zrnica, 2005: The joint polarization experiment: Polarimetric rainfall measurements and hydrometeor classification. *Bull. Amer. Meteor. Soc.*, **86**, 809–824.
- Saunders, C. P. R., and S. L. Peck, 1998: Laboratory studies of the influence of the rime accretion rate on charge transfer during graupel/crystal collisions. *J. Geophys. Res.*, **103D**, 13 949–13 956.
- Takahashi, T., 1978: Riming electrification as a charge generation mechanism in thunderstorms. *J. Atmos. Sci.*, **35**, 1536–1548.
- Thomas, R., P. Krehbiel, W. Rison, J. Harlin, T. Hamlin, and N. Campbell, 2003: The LMA flash algorithm. *Proc. 12th Int. Conf. on Atmos. Electricity*, Versailles, France, ICAE, 655–656.
- , —, —, S. J. Hunyady, W. P. Winn, T. Hamlin, and J. Harlin, 2004: Accuracy of the Lightning Mapping Array. *J. Geophys. Res.*, **109**, D14207, doi:10.1029/2004JD004549.
- Wang, Y., V. Chandrasekar, and B. Dolan, 2008: Development of scan strategy for dual Doppler retrieval in a networked radar system. Preprints, *IEEE Int. Geoscience Remote Sensing Symp.*, Boston, MA, IEEE, V-322–V-325.
- Wiens, K. C., S. A. Rutledge, and S. A. Tessendorf, 2005: The 29 June 2000 supercell observed during STEPS. Part II: Lightning and charge structure. *J. Atmos. Sci.*, **62**, 4151–4177.
- Williams, E. R., 1985: Large-scale charge separation in thunderclouds. *J. Geophys. Res.*, **90D**, 6013–6025.
- , 1989: The triple structure of thunderstorms. *J. Geophys. Res.*, **94D**, 13 151–13 167.
- , 2001: The electrification of severe storms. *Severe Convective Storms, Meteor. Monogr.*, No. 50, Amer. Meteor. Soc., 527–561.
- , C. M. Cooke, and K. A. Wright, 1985: Electrical discharge propagation in and around space charge clouds. *J. Geophys. Res.*, **90D**, 6059–6070.
- , M. E. Weber, and R. E. Orville, 1989: The relationship between lightning type and convective state of thunderclouds. *J. Geophys. Res.*, **94D**, 13 213–13 220.
- , R. Zhang, and J. Rydock, 1991: Mixed-phase microphysics and cloud electrification. *J. Atmos. Sci.*, **48**, 2195–2203.
- , —, and D. Boccippio, 1994: Microphysical growth state of ice particles and large-scale electrical structure of clouds. *J. Geophys. Res.*, **99**, 10 787–10 792.
- Wilson, J. W., R. D. Roberts, C. Kessinger, and J. McCarthy, 1984: Microburst wind structure and evaluation of Doppler radar for airport wind shear detection. *J. Climate Appl. Meteor.*, **23**, 898–915.
- Zink, M., E. Lyons, D. Westbrook, D. Pepyne, B. Philips, J. Kurose, and V. Chandrasekar, 2008: Meteorological command & control: Architecture and performance evaluation. Preprints, *IEEE Int. Geoscience Remote Sensing Symp.*, Boston, MA, IEEE, V-152–V-155.